On the mode of dynamo action in a global large-eddy simulation of solar convection

Étienne Racine

Canadian Space Agency, St-Hubert, Qc, CANADA

Paul Charbonneau, Mihai Ghizaru, Amélie Bouchat

Département de Physique, Université de Montréal, C.P. 6128 Succ. Centre-ville, Montréal, Qc, H3C-3J7 CANADA

Piotr K. Smolarkiewicz

National Center for Atmospheric Research, Boulder, CO 80307, USA

October 25, 2010

ABSTRACT

In this paper we examine the mode of dynamo action in the implicit large-eddy magnetohydrodynamical simulation of solar convection reported upon in Ghizaru *et al.* (2010, ApJL, 715, L133). Motivated by the presence of a strong and well-defined large-scale axisymmetric magnetic component undergoing regular polarity reversals, we define the fluctuating component of the magnetic field as the difference between the total field and it zonal average. The subsequent analysis follows the physical logic and mathematical formulation of mean-field electrodynamics, whereby a turbulent electromotive force (EMF) is computed by suitable averaging of cross-correlations between fluctuating flow and field components, and expressed in terms of the mean-field via a linear truncated tensorial expansion. We use singular value decomposition to perform a linear least-squares fit of the temporal variation of the EMF to that of the large-scale magnetic component, which yields the components of the full α-tensor. Its antisymmetric component, describing general turbulent pumping, is also extracted. The α-tensor so calculated reproduces a number of features already identified in local, cartesian simulations of magnetohydrodynamical rotating convection, including a $\alpha_{\phi\phi}$ component positive in the Northern solar hemisphere, peaking at high latitudes and reversing sign near the bottom of the convection zone; downward turbulent pumping throughout the convecting layer; significant equatorward turbulent pumping at mid-latitudes, and poleward at high latitudes in subsurface layers. We also find that the EMF contributes significantly to the regeneration of the large-scale toroidal magnetic component, which from the point of view of mean-field dynamo models would imply that the simulation operates as an $\alpha^2\Omega$ dynamo. We find no evidence of α-quenching by the large-scale magnetic field. The amplitude of the magnetic cycle appears instead to be regulated primarily by a magnetically-driven reduction of the differential rotation.

The solar magnetic field is the energy source for the whole set of physical phenomena collectively known as "solar activity". While flux emergence is the primary driver on timescales ranging from minutes to months, on longer timescales of years to millenia solar activity is strongly modulated by the solar cycle, namely the cyclic variation of the sun's large-scale magnetic component. This cyclic variation, characterized by polarity reversals approximately every 11 years, is believed to be powered by a magnetohydrodynamical dynamo process operating in the solar interior, within its convective envelope and possibly immediately beneath its interface with the underlying, stably stratified radiative core ($r/R_\odot \simeq 0.71$, according to helioseismic inversions of the solar internal sound speed profile; see, e.g., Christensen-Dalsgaard 2002). A proper understanding of this dynamo process is thus justly recognized as a cornerstone of research into the myriad of manifestations of solar activity.

For physical conditions characteristic of the solar interior, the solar dynamo is expected to be well described by the classical magnetohydrodynamical approximation (e.g., Davidson 2001, Goedbloed & Poedts 2004), a fusion of the hydrodynamical fluid equations and Maxwell's equations applicable to a non-relativistic, globally neutral and collisionally-dominated plasma obeying Ohm's Law. The resulting set of nonlinear, coupled partial differential equations remains daunting, and in general can only be solved numerically. Simplified model formulations based on mean-field electrodynamics (e.g., Moffat 1978; Krause & Rädler 1980; Rüdiger & Hollerbach 2004, and references therein) readily produce cyclic solutions for reasonable though largely *ad hoc* input parameters and key functionals such as the α-effect and turbulent diffusivity (for a recent review see Charbonneau 2010). However, and without at all diminishing their usefulness as descriptive models as well as thinking tools, the freedom to specify free functions, and the highly simplified treatment of the nonlinear interactions between flow and field, poses fundamental limits the applicability of such models to the solar cycle.

Alternately, the dynamo problem can be tackled as a dynamically consistent simulation of thermally-driven magnetohydrodynamical convection in a thick, stratified and rotating spherical shell of electrically conducting fluid (Gilman 1983; Glatzmaier 1984). The resulting computational problem is quite challenging due to the turbulent nature of fluid motions in the solar convection zone, which generates a very wide range of spatial and temporal scales in the evolving flow and magnetic field. For many decades, the computational resources needed to capture dynamo action in a global simulation of the whole solar convection zone has kept this type of simulations at the forefront of computational fluid dynamics, a situation that persists to this day (see Miesch & Toomre 2009 for a review).

Following the development of a massively parallel version of the Glatzmaier (1984) simulation code by Clune *et al.* (1999), a reasonably turbulent regime could be attained. While such turbulent global MHD simulations of solar convection do produce a lot of magnetic field (see, e.g., Brun *et al.* 2004), they often fail to produce magnetic fields well-organized on large spatial scales and carrying a significant net hemispheric flux. Towards this end the introduction of a stable fluid layer underlying the convection zone, where strong, persistent angular velocity shear can develop

in a tachocline-like layer, has been shown to be conducive to the buildup of persistent large-scale magnetic fields (see Browning *et al.* 2006; Ghizaru *et al.* 2010; Käpylä *et al.* 2010); however, at higher rotation rates it appears that the buildup of large-scale magnetic fields can occur entirely within the convective envelope, without a tachocline (Brown *et al.* 2010a,b).

Regular, solar-like cyclic activity has been even harder to produce in such simulations. The groundbreaking simulations of Gilman (1983) and Glatzmaier (1984, 1985) did produce polarity reversals, but computing limitations restricted these simulations to mildly turbulent regimes, while the resulting spatiotemporal evolution of the large-scale magnetic field they produced was non-solar in a number of ways, notably the tendency for latitudinal migration of the large-scale magnetic field to take place poleward rather than equatorward. In the more turbulent, contemporary versions of these simulations, polarity reversals of large-scale magnetic field structures has so far only been produced for rotation rates five times that of the Sun (Brown *et al.* 2010b), with the timing of these reversals markedly asynchronous across hemispheres. Very recently Miesch *et al.* (2011) also reported on the occurrence of a few polarity reversals in a variation on the simulations of Brown *et al.* (2010b) operating now at the solar rotation rate, with better synchrony across hemisphere but a tendency, albeit weak, for poleward migration of the large-scale magnetic component. Operating under an entirely different numerical framework, Käpylä *et al.* (2010) also obtained cyclic large-scale magnetic fields in a spherical wedge simulation spanning up to 120° in longitude, 67° in latitude, and including an underlying stable layer. Those cycling large-scale magnetic fields again are characterized by poleward propagation much as in Gilman (1983), and also show strong hemispheric asymetries.

At this writing the turbulent simulations having produced the most solar-like cyclic large-scale magnetic fields are those presented in Ghizaru *et al.* (2010). Based on a MHD extension of the well-documented general-purpose hydrodynamical simulation code EULAG (Prusa *et al.* 2008; Smolarkiewicz & Szmelter 2009; and references therein), the simulation is based on the hydrodynamical model setup of solar convection described in Elliott & Smolarkiewicz (2002). The temporally extended simulation reported upon in Ghizaru *et al.* (2010) is characterized by a number of encouragingly solar-like features: (1) a well-defined axisymmetric large-scale magnetic field component, antisymmetric about the equatorial plane; (2) magnetic polarity reversals with a half-period of approximately 30 yrs, synchronous across hemispheres, (3) a strong (up to 0.3 Tesla) toroidal component concentrated at the interface between the convecting and underlying stable layers, peaking at mid latitudes and showing a weak but clear tendency for equatorward migration as the cycles unfold; (4) a dipolar component, well aligned with rotation axis and strongly peaked at high latitudes; (5) a reasonably solar-like internal differential rotation, showing equatorial acceleration and vanishing rapidly at the core-envelope interface. The most glaring departures from the observed solar cycle are: the cycle period, three times too long; the fact that the large-scale poloidal and toroidal component oscillate essentially in phase, in contrast to the $\pi/2$ phase lag observed on the sun; and the pole-to-equator contrast in surface angular velocity, too small by a factor of almost three.

We are currently engaged in a systematic numerical exploration of parameter space, in order to answer a number of pressing questions, notably (1) what sets the cycle period in the simulation; (2) why is our simulation producing well-defined, fairly regular cycles while the simulations of, e.g., Browning *et al.* (2006), by all appearances quite similar in overall design and turbulent regime, do not; (3) how robust are the cycles to the manner in which convection is being forced, and the dissipation introduced via the numerical advection scheme. This is a long, tedious and computationally demanding process, which could be greatly accelerated if the physical nature of dynamo action in these simulations could be pinned down with some degree of confidence. Accordingly, the purpose of this paper is to examine the mode of dynamo action in the one specific simulation run presented in Ghizaru *et al.* (2010), which has by now been extended to 337 yr of simulated time, in the course of which 11 polarity reversals have taken place. Our primary aim is to examine the degree (if any) to which dynamo action in this simulation can be described through turbulent effects described by mean-field electrodynamics, as embodied in the α-effect and turbulent pumping. A brief overview of the simulation is first presented in §1, after which we describe the procedure adopted to extract the components of the α-tensor, and what these turn out to look like in our simulation (§2). We then examine (§3) the degree to which large-scale dynamo action in the simulation resembles what one can observe in conventional mean-field dynamo models and examine the relative importance of turbulent induction of the toroidal component versus shearing of the large-scale magnetic component by differential rotation. We close (§4) by summarizing our results and speculating on further improvements that could lead to a better reproduction of the observed characteristics of the solar cycle in this type of MHD simulation.

1. Overview of the simulation

The purpose of this section is to give an overview of the magnetic cycles developing in a temporally extended version of the global MHD simulations of solar convection reported upon in Ghizaru *et al.* (2010). This specific simulation provides the numerical data used in the remainder of this paper in our analysis of large-scale dynamo action.

A brief description of the simulation framework is given in Ghizaru *et al.* (2010), and a detailed presentation will be given in a forthcoming publication. The simulation used in what follows is computed at relatively low spatial resolution ($N_r \times N_\theta \times N_\phi = 47 \times 64 \times 128$), which permits long temporal integrations, yet the low dissipative properties of the underlying EULAG computational framework still yields a reasonably turbulent regime, with estimated Reynolds numbers of order 10^2 and magnetic Prandtl number of order unity. The simulation solves the anelastic form of the ideal MHD equations in a thick, gravitationally stratified spherical shell ($0.62 \leq r/R_\odot \leq 0.96$) spanning 3.4 density scale heights and rotating at the solar rate $\Omega_\odot = 2.69 \times 10^{-6}\,\mathrm{rad\,s^{-1}}$. With the exception of an explicit radiative diffusion term in the energy equation, all dissipation is delegated to the numerical advection scheme MPDATA (Smolarkiewicz 2006), the higher-order truncation terms of which provide an implicit turbulence model (Domaradzki *et al.* 2003; Margolin *et al.* 2006; Margolin

& Rider 2007). The background stratification, defined through a combination of polytropes, is stable below $r/R_\odot = 0.718$, and convection in the overlying layers is driven by a Newtonian forcing towards a weakly convectively unstable thermodynamic profile. This procedure, borrowed from simulation of an idealized terrestrial climate (Held & Surez 1994; Smolarkiewicz *et al.* 2001) is physically equivalent to imposing a heat flux through the fluid layer. The simulation of Ghizaru *et al.* (2010), although subjected to the solar heat flux, is relatively weakly forced from the convection point of view, and ongoing simulations operating under different forcing regimes indicate that large-scale dynamo behavior can be sensitive to details of the forcing. Such sensitivity is not at all unusual in a turbulent fluid system (Piotrowski *et al.* 2010).

Figure 1 shows a temporal sequence of the toroidal (zonal) magnetic component in the simulation, extracted on a spherical shell corresponding to the core-envelope interface ($r/R_\odot = 0.718$ in the simulation), plotted in latitude-longitude Mollweide projection. From top to bottom, the sequence runs from one magnetic maximum to the next, and is temporally centered on a polarity reversal (middle panel). Despite strong fluctuations in the magnetic field, a large-scale axisymmetric component antisymmetric about the equatorial plane is clearly apparent except at the time of polarity reversal. In fact, except for the obvious reversal of magnetic polarity, the magnetic field distributions at top and bottom are remarkably similar, showing concentration at mid-latitudes and comparable peak strenghts ($\sim 0.3\,\mathrm{T}$) in both hemispheres. Polarity reversals occur through a gradual weakening of the large-scale axisymmetric magnetic component, with antisymmetry about the equatorial plane maintained reasonably well as the time of reversal is approached ($t = 202.5\,\mathrm{yr}$), and establishing itself rapidly again once the next half-cycle starts to build up ($t = 221.9\,\mathrm{yr}$).

The spatiotemporal evolution of the large-scale axisymmetric component is best viewed by zonally averaging the total magnetic field present at any given time in the simulation. Working in spherical coordinates (r, θ, ϕ), where $-\pi/2 \leq \theta \leq \pi/2$ is the latitude (rather than the polar angle), such a zonal average is defined as:

$$\langle \boldsymbol{B} \rangle (r, \theta, t) = \frac{1}{2\pi} \int_0^{2\pi} \boldsymbol{B}(r, \theta, \phi, t) \mathrm{d}\phi \tag{1}$$

The top panel on Figure 2 shows a time-latitude diagram of the toroidal magnetic component ($\langle B_\phi \rangle$) averaged in this manner, constructed at a depth corresponding to the core-envelope interface in the model ($r/R_\odot = 0.718$). If the toroidal magnetic flux ropes assumed to give rise to bipolar active regions are indeed stored at this depth, as suggested by stability analyses (e.g., Ferriz-Mas *et al.* 1994; Fan 2009), and rise radially to the photosphere, then this is the simulation's equivalent to the sunspot butterfly diagram (e.g., Hathaway 2010). The toroidal magnetic component is concentrated at mid-latitudes ($40^\circ \leq |\theta| \leq 70^\circ$), as opposed to the low latitudes ($5^\circ \leq |\theta| \leq 40^\circ$) suggested by the butterfly diagram, but does show a tendency for equatorial migration as each half-cycle unfolds. On a time-latitude diagram such as Fig. 2 (top panel), this is seen in the strong toroidal field concentrations, which take an elongated, elliptical shape, with the "major axis" tilted towards the equator as the cycle is followed in time. In other words, throughout a cycle the latitude

of peak large-scale toroidal magnetic field occurs at decreasing latitudes, until the cycle terminates and the next one begins anew at higher latitudes.

The middle panel of Figure 2 shows time-radius slice of the same simulation run, extracted in the southern hemisphere at latitude $-45°$, where the toroidal field is strongest at the core-envelope interface (cf. top panel). Note how polarity reversals begin well within the convection zone, at depth $r/R_\odot \simeq 0.8$, with radial drift and concentration of the magnetic field both upwards as well as downwards all the way to the core-envelope interface, where the field reaches its peak strength.

The bottom panel of Figure 2 shows the corresponding time-evolution of the zonally-averaged radial surface magnetic component, again in a time-latitude diagram. The surface field is characterized by a well-defined dipole moment closely aligned with the rotational axis, with transport of surface fields taking place from lower latitudes, and possibly contributing to the reversal of the dipole moment. Comparing the three panels in Fig. 2 reveals that the dipole moment and deep-seated toroidal component reach their peaks at the same time, indicating that they oscillate in phase, without significant temporal lag.

Overall, the magnetic cycle characterizing the large-scale, zonally-averaged magnetic component is quite regular, here with a half-period of 30 years, almost thrice the 11 years of the solar cycle. Notice the good long-term synchrony maintained between the Northern and Southern hemispheres, persisting despite significant fluctuations in the amplitude and duration of cycles in each hemiphere. In keeping with solar tradition, we delineate the cycles from one polarity reversal to the next. Note therefore that what we henceforth refer to as "cycle", as numbered on the bottom panel of Fig. 2, span in fact one half of a complete magnetic cycle. While the average period of our cycles so defined is almost exactly 30 yr for our 11 cycles, this period can become as low as 25 yr (simulated cycle 11) or as high as 35 (simulated cycle 4) from one cycle to the next.

2. Mean-field analysis

2.1. Scale separation and averages

Mean-field electrodynamics is predicated on the *assumption* that the fluid flow ($\boldsymbol{u}$) and magnetic field ($\boldsymbol{B}$) can be separated into "mean" (usually spatially large-scale and slowly varying in time) and "fluctuating" (usually small-scale and rapidly varying) components:

$$\boldsymbol{u} = \langle \boldsymbol{u} \rangle + \boldsymbol{u}' \ , \qquad \boldsymbol{B} = \langle \boldsymbol{B} \rangle + \boldsymbol{B}' \ , \tag{2}$$

where the angular brackets denote an intermediate averaging scale for which

$$\langle \boldsymbol{u}' \rangle = 0 \ , \qquad \langle \boldsymbol{B}' \rangle = 0 \ . \tag{3}$$

Given the well-defined large-scale axisymmetric component present in our simulation, it becomes natural to associate the averaging scale with the zonal average defined through Eq. (1), so that the

fluctuating components become *defined* as:

$$\boldsymbol{u}'(r,\theta,\phi,t) = \boldsymbol{u}(r,\theta,\phi,t) - \langle \boldsymbol{u} \rangle (r,\theta,t) \ , \tag{4}$$

$$\boldsymbol{B}'(r,\theta,\phi,t) = \boldsymbol{B}(r,\theta,\phi,t) - \langle \boldsymbol{B} \rangle (r,\theta,t) \ . \tag{5}$$

In practice, it is of course possible to define fluctuating flows and fields in this way for any global MHD simulation run. However, for the mean-field electrodynamics approach to be mathematically well-posed and physically meaningful, it is essential for a good separation of scales to hold. Accordingly, we first examine in some detail whether this is indeed the case for our simulation.

Figure 3 shows the mean and fluctuating toroidal magnetic field components resulting from this decomposition applied to the toroidal field distribution plotted on the bottom panel of Fig. 1 (simulation time $t = 230\,\mathrm{yr}$, very near the peak of simulated cycle 8). At the base of the convection zone, both components have similar strength, but the fluctuating component on Fig. 3 shows little or no azimuthal structuring on scales comparable to the solar radius, nor any clear hemispheric pattern. In particular, no sign of a significant non-axisymmetric dipolar or quadrupolar components is visible.

This visual impression is confirmed by a modal decomposition in spherical harmonics, which reveals significant power concentrated in axisymmetric ($m = 0$) mode of low, odd angular degree ℓ. This is illustrated on Figure 4, showing the result of a spherical harmonic decomposition of the toroidal magnetic component at the core-envelope interface ($r/R_\odot = 0.718$). The decomposition was carried out at every time step, and then averaged for two sets of disjoint data blocks of temporal width 900 days centered either on the epochs of polarity reversals (panel A, "cycle minima"), or peak toroidal field (panel B, for "cycle maxima"). The results are displayed in the form of color coding of the absolute values of the modal coefficients, in the plane defined by the angular degree ℓ (horizontal) and azimuthal degree m (vertical). The diamond shape results from the usual triangular truncation of azimuthal modes, needed to ensure comparable spatial resolution in the latitudinal and azimuthal directions.

Comparing panels A and B of Figure 4 reveals significant power in the axisymmetric ($m = 0$) angular modes of odd-ℓ angular degree at cycle maximum, that all but vanish at times of cycle minimum. This is particularly prominent for the dipolar $(\ell, m) = (1, 0)$ mode. At high-ℓ values, on the other hand, power is broadly and more evenly distributed in modes of all azimuthal orders m, and shows no clear variations with the phase of the cycle for the large-scale field. Indeed, subtracting panel B from panel A, yielding panel C on Figure 4, reveals very little residual power at high wavenumbers. This indicates that the cycle in the large-scale axisymmetric magnetic field does not alter significantly the spectral properties of the small-scale, "turbulent" magnetic component.

A different look at these data is presented on Figure 5, which shows time series of a few selected spherical harmonic coefficients, spanning the full simulation run. The cycle shows up prominently in the $(\ell, m) = (1, 0)$ and $(5, 0)$ modes, but the time series for $m \neq 0$ modes, as well as for even-ℓ

axisymmetric modes, have much lower amplitudes and show no sign of persistent cyclic variation. This has been further verified by computing Fourier transforms of these various time series, which show clear peaks at periods of ~ 29 and $\sim 58\,\mathrm{yr}$ in the odd-ℓ axisymmetric modes, but no peaks and overall power levels inferior by over an order of magnitude for even-ℓ and $m \neq 0$ modes. Similar temporal patterns are observed within the convection zone and/or for the other magnetic components. Overall, the above analyses then suggest that the decomposition embodied in Eqs. (4) and (5) represents a viable *Ansatz*, at least for this simulation run.

2.2. The turbulent electromotive force

With the assumption of scale separation vindicated at least to some degree, our purpose is now to identify and characterize the dynamo mechanism underlying the observed magnetic cycle described above. The starting point of the analysis is the magnetohydrodynamical induction equation (e.g., Davidson 2001), describing the evolution of a magnetic field $\boldsymbol{B}$ subjected to the inductive action of a flow field $\boldsymbol{u}$ in addition to Ohmic dissipation of the associated electrical current density:

$$\frac{\partial \boldsymbol{B}}{\partial t} = \boldsymbol{\nabla} \times \Big[\boldsymbol{u} \times \boldsymbol{B} - \eta \boldsymbol{\nabla} \times \boldsymbol{B} \Big] , \tag{6}$$

where $\eta = (\mu_0 \sigma_e)^{-1}$ is the magnetic diffusivity, inversely proportional to the electrical conductivity σ_e (SI units are used throughout). Inserting Eqs. (2) and performing the zonal average introduced earlier, and remembering that the averaging operator commutes with spatial derivatives pertaining to the large spatial scales, one readily obtains:

$$\frac{\partial \langle \boldsymbol{B} \rangle}{\partial t} = \boldsymbol{\nabla} \times \Big[\langle \boldsymbol{u} \rangle \times \langle \boldsymbol{B} \rangle + \boldsymbol{\mathcal{E}} - \eta \boldsymbol{\nabla} \times \langle \boldsymbol{B} \rangle \Big] , \tag{7}$$

where

$$\boldsymbol{\mathcal{E}} = \langle \boldsymbol{u}' \times \boldsymbol{B}' \rangle \tag{8}$$

is the mean electromotive force (hereafter EMF) due to the fluctuations about the large scale magnetic field. Note that this mean turbulent EMF is generally nonzero, because the correlation between the fluctuating flow and magnetic field does not necessarily vanish upon averaging, even though $\boldsymbol{u}'$ and $\boldsymbol{B}'$ individually do by definition. For more details on some of the many subtleties involved, see, e.g., Moffatt (1978); Rüdiger & Hollerbach (2004), Hoyng (2003), Ossendrijver (2003).

From the simulation results, it is straightforward to reconstruct $\boldsymbol{u}'$ and $\boldsymbol{B}'$ via Eqs. (4) and (5), and then compute the EMF by performing the required cross product and zonal averaging at every time step, as per Eq. (8). The result of this calculation is presented on Figure 6 for the r (top), θ (middle) and ϕ (bottom) components of the EMF, in the form of time-latitude slices at depth $r/R_\odot = 0.85$ near the middle of the convection zone (left panels), where polarity reversals are initiated (see Fig. 2), and meridional slices extracted at simulation time $t = 112\,\mathrm{yr}$, at the peak of the fourth magnetic half-cycle (right panels). Note already how the EMF vanishes rapidly as one moves below the core-envelope interface, as expected since convectively-driven turbulence

disappears there. Otherwise the EMF pervades most of the convection zone. Despite being a very noisy "signal", on the largest spatial scales all EMF components exhibit a well-defined symmetry ($\mathcal{E}_r$, $\mathcal{E}_\phi$) or antisymmetry ($\mathcal{E}_\theta$) about the equatorial plane. Note in particular that a ϕ-component of the EMF positive (negative) in both hemisphere is precisely what is required to support a positive (negative) dipole moment (cf. bottom panels on Figs. 2 and 6), as per the right-hand rule, since under the MHD approximation the EMF drives an parallel electrical current density. Moreover, reversing the direction of this EMF every half-cycle then amounts to reversing the sign of that dipole moment, as observed in the simulation.

All EMF components show strongly reduced amplitudes in the equatorial regions. This can be traced to a change in the topological character of convective fluid motions, which at low latitudes tend to organize themselves in longitudinal stacks of large, latitudinally-elongated convective cells approximately aligned with the rotational axis (see Fig. 1A in Ghizaru *et al.* 2010). These are quite typical of these types of global convection simulations (see, e.g., Browning *et al.* 2006, Fig. 1; Brown *et al.* 2010, Fig. 1; Käpylä *et al.* 2010, Fig. 2). Evidence of a quenching of the small-scale flow components can also be found in the spatial distribution of the small-scale surface magnetic field, which shows a significant decrease in both coverage and magnitude at very low latitudes (see, e.g., Fig. 1B in Ghizaru *et al.* 2010).

The most striking global spatiotemporal feature visible on Fig. 6 is certainly the cyclic variation of all EMF components, with a period identical to that of the cycle observed in the large-scale magnetic field (cf. Fig. 2). Here the large-scale velocity field is roughly stationary over the entire simulation, and the small-scale turbulent velocity field is also stationary in a statistical sense. Since the EMF term depends only on the small-scale fluctuations about the large scale magnetic fields, it is then not at all obvious *a priori* that the EMF should exhibit the same cyclic evolution as the mean-field; the fact that it does already provides us with important clues as to the nature of the large-scale dynamo operating in our simulation. More specifically, it suggests that the turbulent EMF actually plays a key role in the *production* of the large-scale magnetic component. We now turn to this question, using the mathematical machinery of mean-field electrodynamics.

2.3. The α-tensor

The essence of mean-field electrodynamics is to provide an expression for the EMF in terms of the large scale magnetic field, so that the small scales (fluctuations) are effectively removed from the problem. The procedure consists of a simple linear expansion of the EMF as a power series about the large-scale magnetic field and its derivatives, i.e.

$$\mathcal{E}_i = \alpha_{ij}\langle B_j\rangle + \beta_{ijk}\partial_j\langle B_k\rangle + \text{ higher order derivatives }, \tag{9}$$

with summation implied over repeated indices. The tensors appearing on the RHS of this expression and relating the EMF to the mean-field can depend on the properties of small-scale flow and field fluctuations, but *not* on the mean field itself, a situation expected to hold only if the latter is too

weak to impact the dynamics of the fluctuating flow. Notice here that since this expansion is linear in the large-scale field, if that field exhibits cyclic properties, then so should the EMF, which is what we observe (cf. Fig. 6). This is our central motivation for appealing to mean-field electrodynamics to analyze the dynamo operating deep in the convection zone of our simulation.

The leading-order contribution in the right-hand side of Eq. (9) is usually named "α-effect". The second term in the expansion is responsible, among other effects, for turbulent diffusion. For our first analysis however, we retain only the α-effect for simplicity. Owing to the rough stationarity of the large-scale flows in the simulation, we also assume that α_{ij} is time-independent, an assumption that will prove itself well-verified *a posteriori*. We thus write, as a first approximation

$$\mathcal{E}_i(t, r, \theta) = \alpha_{ij}(r, \theta)\langle B_j\rangle(t, r, \theta)\,. \tag{10}$$

One can further decompose α_{ij} into symmetric and antisymmetric parts, such that the EMF may be rewritten as

$$\mathcal{E}_i = \alpha_{(ij)}\langle B_j\rangle + \Big(\boldsymbol{\gamma} \times \langle \boldsymbol{B}\rangle\Big)_i\,, \tag{11}$$

where

$$\gamma_i = -\frac{1}{2}\epsilon_{ijk}\alpha_{jk} \tag{12}$$

is called the general turbulent pumping velocity, because it effectively provides an additive contribution to the mean, large-scale inductive flow in Eq. (7), although its physical origin lies with the fluctuating, small-scale flow and magnetic field. The flow-like vector field $\boldsymbol{\gamma}$ so-defined is in general non-solenoidal ($\nabla \cdot \boldsymbol{\gamma} \neq 0$) and acts on the total magnetic field, with variations between magnetic component subsumed into the off-diagonal terms of the symmetric part of the α-tensor (see Ossendrijver et al. 2002 for a more thorough discussion).

2.4. Extracting the components of the α-tensor

A number of methods have been designed to measure the components of the α-tensor in turbulent MHD simulations (e.g., Ossendrijver *et al.* 2001, 2002; Käpylä *et al.* 2006, 2009; Hubbard *et al.* 2009; and references therein). These method have been designed in the context of MHD simulations that do not produce a well-defined large-scale magnetic component, so that the latter must be imposed externally —and artificially,— with the consequence that the α-tensor being measured is not necessarily that characterizing the simulation prior to the application of the external field. For more on these —and other— difficulties, see Brandenburg (2009), Cattaneo & Hughes (2009), and references therein. In contrast, we are in the very advantageous position to have in hand a simulation that does generate a large-scale magnetic field, in a manner consistent with the dynamical interaction of flow and field on all numerically resolved spatial scales.

The procedure we employ here to extract α_{ij} from the simulation data differs from the approaches found in the literature, and we shall therefore first detail it. Essentially, we attack this problem from an experimentalist's point of view, i.e., we have (numerical) data in our possession,

namely the EMF and the average magnetic field, and we wish to verify if these data match a specific model, namely the α-effect parametrization of the EMF embodied in Eq. (10). This task therefore amounts to a fitting problem, in other words the components of the tensor α_{ij} are calculated *a posteriori* by minimizing the difference between the LHS and RHS of Eq. (10). We opt here for a standard least squares fit, based upon singular value decomposition (see Press *et al.* 1992, §15.4). We state results of various theorems without proof.

For a given component, say $i = a$, of the EMF at a fixed grid point[1] (r_b, θ_c), we define the time dependent functions $y(t)$ and $X_k(t)$ as follows

$$y(t) = \mathcal{E}_a(t, r_b, \theta_c)\,, \tag{13a}$$

$$X_k(t) = \langle B_k \rangle(t, r_b, \theta_c)\,. \tag{13b}$$

We also define

$$a_k = \alpha_{ak}(r_b, \theta_c)\,, \tag{14}$$

which then allows us to rewrite the parametrization of the EMF as

$$y(t) = \sum_{k=1}^{3} a_k X_k(t)\,. \tag{15}$$

Denoting by n_t the number of time steps of our simulation, we define a merit function as

$$\chi^2 = \sum_{i=1}^{n_t} \left[y(t_i) - \sum_{k=1}^{3} a_k X_k(t_i) \right]^2, \tag{16}$$

where t_i is the value of the time coordinate at the i^{th} step. The goals are to find the three parameters a_k that minimize the merit function, and to obtain an estimate of the goodness of fit. The method we employ to carry out these two tasks simultaneously is the singular value decomposition of the "design matrix" $\mathbf{A}$, defined as

$$A_{ij} = X_j(t_i)\,. \tag{17}$$

The design matrix therefore depends on the large scale magnetic field components. This matrix has n_t rows and three columns, and by virtue of a theorem of linear algebra, can always be decomposed as follows

$$\mathbf{A} = \mathbf{U} \cdot \mathbf{w} \cdot \mathbf{V}^T\,, \tag{18}$$

where the matrix $\mathbf{U}$ is an n_t-by-three column orthogonal matrix, $\mathbf{w}$ is a three-by-three diagonal matrix containing the so-called "singular values", and $\mathbf{V}$ is a three-by-three orthogonal matrix. The key element is that the solution to the minimization of the merit function (16) is directly obtained in terms of the three matrices $\mathbf{U}$, $\mathbf{V}$ and $\mathbf{w}$. The solution vector $\boldsymbol{a} = (a_1, a_2, a_3)$ is given by

$$\boldsymbol{a} = \mathbf{V} \cdot \mathbf{w}^{-1} \cdot \mathbf{U}^T \cdot \boldsymbol{y}\,, \tag{19}$$

[1]Since the quantities considered in this section are constructed from azimuthal averages, our computational grid is reduced to two spatial dimensions here.

where the vector $\boldsymbol{y} = (y_1, y_2, ..., y_{n_t})$, and therefore depends on the selected EMF component. To construct the singular value decomposition of our design matrix, we use the algorithm and routines of Press *et al.* (1992), as implemented in the IDL programming language. By repeating this procedure for all three components of the EMF and for each of the $N_r \times N_\theta$ grid points (r_b, θ_c), we can calculate the complete tensor $\alpha_{ij}(r, \theta)$.

Figure 7 shows the results of this fitting procedure over the complete 337 year simulation interval. Each meridional slice encodes one component of the α-tensor, or combinations thereof. The 3×3 structure of the subfigures reflects the 3×3 components of the tensor, with the top-left to bottom-right diagonal corresponding to the diagonal components α_{rr}, $\alpha_{\theta\theta}$ and $\alpha_{\phi\phi}$. The three meridional slice above this diagonal (top right) correspond to the off-diagonal elements of the symmetric part of the α-tensor (indices within parentheses), while the three plots below the diagonal represent the three independent components of the antisymmetric part of the tensor, plotted here as components of the turbulent pumping velocity γ defined through Eq. (12). To facilitate comparison, the same color scale is used on all meridional slices.

Although all components of the α-tensor are roughly of the same order of magnitude, the strongest components are found to be α_{rr} and $\alpha_{\phi\phi}$, both antisymmetric about the equatorial plane. The former is highly structured spatially, peaking in subsurface layers and in the equatorial regions and with numerous sign changes in each hemisphere. The latter is spatially more homogeneous, with sign changes only across the equatorial plane and across a near-spherical surface located above the core-envelope interface, at $r/R \simeq 0.76$. Significant amplitudes are obtained in the off-diagonal contributions, particularly $\alpha_{(r\theta)}$ and its associated pumping velocity γ_ϕ. This can be traced to the development of persistent non-axisymmetric flow structures in the low-latitude portions of the outer convection zone (see Fig. 2 in Ghizaru *et al.* 2010), which contribute a strong signal to the "small-scale" flow component even after the azimuthally-averaged mean-flow is subtracted (viz. Eq. (4)). These flow structures are also responsible for the strong low-latitude signal seen in α_{rr}.

The $\alpha_{\phi\phi}$ component is of particular interest here, as it is the primary contributor to the production of the large-scale poloidal magnetic component (cf. bottom panel on Fig. 2). Its first important structural property is antisymmetry with respect to the equatorial plane, as expected for cyclonic turbulence, where reflectional symmetry is broken by Coriolis forces (Parker 1955). Note that the fitting method we use to measure the components of the α-tensor treats each hemisphere independently, so that the high degree of antisymmetry observed here is a real characteristic of the simulation, rather than a fitting artefact. In the Northern hemisphere, the $\alpha_{\phi\phi}$ component is positive in the bulk of the convection zone and peaks at high latitudes, as expected in view of the sense of twist imparted by Coriolis forces on diverging convective updrafts and converging downdrafts (Parker 1955). The sign change near the base of the convecting layer has been observed before in measurements of the α-tensor in other MHD simulations of convection (e.g., Ossendrijver *et al.* 2001), and is associated with the rapid decrease of the turbulent intensity as one moves downwards towards and into the convectively stable fluid layer underlying the convection zone.

The singular value decomposition method has the additional advantage to automatically provide the variance in the estimate of a given parameter a_k. Denoting this variance by σ_k^2, it is given by

$$\sigma_k^2 = \sum_{i=1}^{3} \left(\frac{V_{ki}}{w_{ii}} \right)^2 . \tag{20}$$

In Fig. 8 (panel B), we show the standard deviation (square root of variance) $\sigma_{\phi\phi}$ corresponding to the fitted parameter $\alpha_{\phi\phi}$, reproduced on part A. For $r < 0.72\,R_\odot$, we set the variance to zero since in the stable zone below the convective zone in order to clearly display the structure of the standard deviation in the convective zone. The reason behind this manipulation is that the EMF and large scale magnetic field are both very weak below the convective zone, reducing greatly the quality of the fit in that region[2]. Figure 8 indicates that even though $\alpha_{\phi\phi}$ peaks at high latitudes, the absolute quality of the fit is actually best at mid-latitudes, where the EMF signal is strongest (see Fig. 6), as expected. Nonetheless, at mid-convection zone depth the inferred values of $\alpha_{\phi\phi}$ in polar regions deviate from zero by more than three standard deviations, leaving no doubt that these values are physically meaningful. On the other hand, in the equatorial region delimited by $|\theta| \lesssim 30^\circ$ and $0.7 \lesssim r/R_\odot \lesssim 0.8$ the standard deviation is of the same order of magnitude as $\alpha_{\phi\phi}$, indicating a poorer fit in that area. This is simply due to the fact that both the EMF and the toroidal large-scale field are small in that region, as can be seen on Figs. 2A and 6.

While the variance of the fit provided by the singular value decomposition is a useful, well-defined tool to characterize the accuracy of the fit, other methods can provide complementary information regarding the parametrization of the EMF. Here we demonstrate the quality of the fit by looking at the ability of the α-effect parametrization to reproduce the observed EMF from the α tensor and the large-scale magnetic field. In Fig. 9A, we plot a time-latitude diagram of the residual between the observed EMF and the reconstructed EMF, i.e. the quantity

$$\Delta_\phi = \mathcal{E}_\phi - \alpha_{\phi j} \langle B_j \rangle \ , \tag{21}$$

computed at depth $r/R_\odot = 0.85$. It is quite remarkable to see that essentially no cyclic features remain in Δ_ϕ. Apart from the equatorial band where the EMF barely manifests itself, there are in fact no clearly discernible structures in Δ_ϕ. This implies that the α-effect parametrization performs very well at capturing the origin of the cyclic features of the EMF, the remainder of the EMF being essentially turbulent noise. This visual impression is confirmed by averaging latitudinally and performing a Fourier transform of the resulting time series, to produce the power spectrum plotted on Figure 9B. This spectrum is well represented by a shallow power law with logarithmic slope $-2/3$, and the spectrum does not show any particular features or changes in slope at frequencies corresponding to the cycle period of the large-scale field or its first few harmonics.

[2]Essentially, where both the EMF and $\langle \boldsymbol{B} \rangle$ are weak, the fitting algorithm attempts to obtain α_{ij} by inverting a problem that is numerically ill-posed. Schematically this amounts to solving $\alpha = \delta/\epsilon$, with α of order unity, but δ and ϵ being very small.

2.5. Turbulent pumping

The three meridional slices under the diagonal on Figure 7 represents the components of the turbulent pumping speed, as defined through Eq. (12). The vertical component γ_r is found to be negative through most of the convective envelope, with upward pumping taking place only in the subsurface layers. This is better viewed on Figure 10 showing radial cuts of γ_r extracted at latitude $+45°$ (panel A, solid line), and latitudinal cuts extracted at depth $r/R_\odot = 0.75$ (panel B). This is qualitatively similar to the results obtained by Ossendrijver *et al.* (2002; see their Fig. 5) in their local cartesian simulations including rotation[3]. This downward pumping reaches significant speeds, $\sim 1\,\mathrm{m\ s^{-1}}$ in the bottom half of the convective layers, except at very low latitudes where it all but vanishes. Upwards pumping occurs at all latitudes for $r/R_\odot \geq 0.9$, except at very low latitudes $|\theta| \leq 15°$), where the $\gamma_r > 0$ region reaches almost to the base of the convecting layer (see Fig. 7, central bottom meridional slice).

We also detect in our simulation a significant equatorward latitudinal pumping in the outer two thirds of the convective envelope (see bottom left meridional slice on Fig. 7 and dotted lines on Fig. 10A and B), particularly prominent at mid-latitudes where it reaches $\sim 1\,\mathrm{m\ s^{-1}}$ in the middle of the convection zone. Both the direction and magnitude of this latitudinal pumping velocity are similar to those measured in the local simulations of Ossendrijver *et al.* (2002). Again like these authors, we also observe significant poleward latitudinal pumping in the subsurface layers of the simulations, with speeds approaching 2 m $\mathrm{s^{-1}}$ at latitude $|\theta| \simeq 60°$. Given the $\sim 30\,\mathrm{yr}$ duration of our cycles, it is therefore quite possible that the poleward drift and intensification of the surface magnetic field seen on the bottom panel of Fig. 2 is driven at least in part by turbulent pumping, as proposed already by Ossendrijver *et al.* (2002).

It is also interesting to compare the turbulent pumping velocity to the drift speed of the large-scale toroidal magnetic field visible on the top and middle panels of Figure 2. The net drift speed of large-scale magnetic structures is influenced by other physical processes, notably turbulent diffusion. Indeed, if turbulent pumping plays a role in this drift its speed should still have values of the same overall order-of-magnitude as to the observed drift speeds. For most cycles, the equatorial drift of the toroidal component at the core-envelope interface (Fig. 2, top panel), as measured by tracking the latitude of peak mean toroidal magnetic field at any given time, spans 25 to 30 degrees in 20 to 25 yr years, depending on individual cycles. This yields drift speeds in the range 0.3–0.5 m $\mathrm{s^{-1}}$. Both the magnitude and direction of this drift compare well to the mid-latitude latitudinal turbulent pumping speed $|\gamma_\theta| \simeq 0.2\,\mathrm{m\ s^{-1}}$ at $r/R_\odot = 0.718$, as plotted on Fig. 10A. Likewise, measuring the slope from $r/R_\odot = 0.8$ to 0.7 of the polarity reversal line on the middle panel of

[3]Note that although we both use right-handed coordinate systems, the pseudo-radial z-direction in Ossendrijver *et al.* (2003) points into the domain, while our radial r-direction points outwards; therefore, a positive γ_r does correspond to a radially upwards flow component in our simulation, while a positive γ_z defines a downward flow in Ossendrijver *et al.* (2003). Our respective "latitudinal" units vectors are however oriented in the same way, i.e. Northward, so that our γ_θ is directly comparable to their γ_x.

Fig. 2 leads to a radial drift speed $\sim -0.1\,\mathrm{m\ s^{-1}}$, only a factor of five smaller than the mid-latitude values of γ_r in this range of depth, as plotted on Fig. 10A. All of this suggests that turbulent pumping may well play an important role in the spatiotemporal evolution of the large-scale, mean magnetic field building up in the simulation.

2.6. α-quenching and cycle amplitude saturation

We next turn our attention to the possible time-dependence of the tensor α_{ij}. Our entire analysis so far relies on the assumption that α_{ij} depends only on position and not time. As we have just shown, this hypothesis works fairly well in practice, in the sense that it provides an accurate parametrization of the electromotive force in terms of the large scale magnetic field. At a more physical level, there are however reasons to believe that the α-effect could vary in time via a nonlinear dependence on the magnetic field strength.

In the solar context, the α-effect can arise via the systematic twist imparted by cyclonic convection on a pre-existing large-scale magnetic field. This idea was introduced by Parker (1955), who argued that it could circumvent Cowling's theorem by providing a viable regeneration mechanism for the sun's large-scale poloidal magnetic component. Because magnetic tension should tend to resist any twisting by the flow, it has been argued that Parker's mechanism can only operate up to the point where the large-scale magnetic field reaches local equipartition with the turbulent fluid motions. This has led to the introduction of a number of simple so-called α-quenching algebraic formulae, e.g.,

$$\alpha_{ij} = \frac{\alpha^0_{ij}}{1 + (\langle B_j \rangle / B_{\mathrm{eq}})^2} \ , \tag{22}$$

where B_{eq} is the equipartition magnetic field strength (see also Rüdiger & Kitchatinov 1993).

In order to explore if the α-effect varies from one cycle to the next, in a manner related to the strength of the mean magnetic field, we refine our analysis by breaking up the simulation data into contiguous blocks each spanning one quarter of a full magnetic cycle. One set of blocks is centered on time of cycle maximum, when the large-scale magnetic field reaches peak strength, and a second set of interweaved blocks are centered on times of polarity reversals, where the large-scale magnetic component reaches its minimum. Because of the regularity of the cycles in the simulations (see Fig. 2), and of the fact that the mean poloidal component oscillates essentially in phase with the mean toroidal component, such a partition of the simulation can be unambiguously defined and readily carried out. We then apply the fitting procedure described previously to each block of data independently, which yields a sequence of functions $\{\alpha_{ij}(r, \theta, t_c)\}$, where t_c is the time around which a given half-cycle is centred. To display the results of this calculation as concisely as possible, for

each t_c we calculate the spatially-averaged quantities α_c and σ_c defined as follows

$$\alpha_c = \frac{1}{V}\int_{r_{min}}^{r_{max}}\int_{hem.} \alpha_{\phi\phi}(r,\theta,t_c)\, r^2 \cos\theta \, dr \, d\theta \,, \tag{23a}$$

$$\sigma_c = \frac{1}{V}\int_{r_{min}}^{r_{max}}\int_{hem.} \sigma_{\phi\phi}(r,\theta,t_c)\, r^2 \cos\theta \, dr \, d\theta \,, \tag{23b}$$

where r_{min} and r_{max} are chosen to include the convective zone, but not the stable zone nor the surface of the simulation, in order to capture the contributions from regions where the α-effect is expected to operate substantially. The quantity V is the total integration volume. The latitudinal integration is restricted to either the north or south hemisphere (to avoid uninteresting cancellations, as the sign of $\alpha_{\phi\phi}$ flips from one hemisphere to the other). The results of those calculations are displayed in Fig. 11, where each histogram-type column represents one half-cycle. The total width of error bars is given by $2\sigma_c$. Although the error bars are quite large[4], the actual values of α_c do not vary substantially at all in both hemispheres throughout the entire simulation. Similar results are obtained for the other components of the α-tensor. The $\alpha_{\phi\phi}$ component does show a very weak ($r = -0.27$) anticorrelation with the mean magnetic field strength, but even there the range of variation is only about one quarter of the standard deviation. All this seems to indicate that there is no significant α-quenching occurring in our simulation, i.e. the value of $\alpha_{\phi\phi}$ is insensitive to the value of the large-scale magnetic field.

3. Relationship to mean-field dynamo models

The scale separation and azimuthal averaging introduced earlier jointly form the basis of the so-called mean-field dynamo models, which have been and continue to be used extensively in studying solar and stellar magnetic activity cycles. If one assumes at the onset that the large-scale magnetic field $\langle \boldsymbol{B} \rangle$ is axisymmetric, then it can be expressed as the sum of a toroidal component and poloidal component defined through a purely azimuthal axisymmetric vector potential $\langle \boldsymbol{A} \rangle = \langle A_\phi \rangle \hat{\mathbf{e}}_\phi$, as:

$$\langle \boldsymbol{B} \rangle (r,\theta,t) = \langle B_\phi \rangle (r,\theta,t)\hat{\mathbf{e}}_\phi + \nabla \times \left(\langle A_\phi \rangle (r,\theta,t)\hat{\mathbf{e}}_\phi \right) \,. \tag{24}$$

One can further assume that the mean flow is also axisymmetric, and comprised only of differential rotation, i.e.,

$$\langle \boldsymbol{u} \rangle (r,\theta,t) = \varpi \Omega(r,\theta,t)\hat{\mathbf{e}}_\phi \,, \tag{25}$$

where $\varpi \equiv r\cos\theta$ and Ω is the (axisymmetric) angular velocity. Under those assumptions, Eq. (7) for the mean field is then readily separated as:

$$\frac{\partial \langle A_\phi \rangle}{\partial t} = \eta \left(\nabla^2 - \frac{1}{\varpi^2} \right) \langle A_\phi \rangle + \mathcal{E}_\phi \,, \tag{26}$$

[4]Since $\alpha_{\phi\phi}(r,\theta,t_c)$ is constructed from a substantially smaller data set (200 time steps) than the full $\alpha_{\phi\phi}$ shown in Fig. 8, which is extracted from the full time span of the simulation, it is no surprise that the variance associated with $\alpha_{\phi\phi}(r,\theta,t_c)$ is much larger than that associated with the full $\alpha_{\phi\phi}$. This explains why the error bars are so large in Fig. 11.

$$\frac{\partial \langle B_\phi \rangle}{\partial t} = \eta \left(\nabla^2 - \frac{1}{\varpi^2} \right) \langle B_\phi \rangle + \varpi [\nabla \times (\langle A_\phi \rangle \hat{\mathbf{e}}_\phi)] \cdot \nabla \Omega + \hat{\mathbf{e}}_\phi \cdot [\nabla \times \boldsymbol{\mathcal{E}}] \ , \tag{27}$$

for constant η and under the Coulomb gauge $\nabla \cdot \langle \boldsymbol{A} \rangle = 0$.

Equations (26)–(27) are known as the mean-field dynamo equations, and models based on these equations (or variations thereof) remain to this day the workhorse of solar cycle modelling, interpretation, and even prediction (see, e.g., Charbonneau 2010, and references therein). They show the critical importance of the mean electromotive force in such axisymmetric mean-field models; the EMF provides a source term on the RHS of the evolution equation for $\langle A_\phi \rangle$, without which dynamo action is impossible, as per Cowling's theorem. It also provides a source term for the toroidal component $\langle B_\phi \rangle$, but here it is less crucial because differential rotation already provides a source contribution, provided a poloidal magnetic component is present. The so-called $\alpha\Omega$ dynamo model results from dropping the α-effect term in Eq. (27), while dropping instead the differential rotation shearing term yields the α^2 model, in which the turbulent EMF is the sole inductive mechanism. Keeping both terms leads to the $\alpha^2\Omega$ mean-field dynamo model.

3.1. Contributions to toroidal field induction

To which (if any) of these three possible mean-field model categories could we identify our simulation? The answer clearly hinges on the relative importance of the $\langle \boldsymbol{u} \rangle \times \langle \boldsymbol{B} \rangle$ and $\langle \boldsymbol{u}' \times \boldsymbol{B}' \rangle$ on the right-hand side of the mean-field induction equation (7). In keeping with our "experimental" approach, we simply use the mean and fluctuating flow and magnetic field components defined previously do directely calculate, using simple centered finite differences, the azimuthal components of both $\nabla \times (\langle \boldsymbol{u} \rangle \times \langle \boldsymbol{B} \rangle)$ and $\nabla \times \langle \boldsymbol{u}' \times \boldsymbol{B}' \rangle$, which then measures the rate of change of the magnetic field associated with each inductive contribution.

Figure 12 shows the results of this exercise, in the form of time-latitude diagrams for the azimuthal component of each of these two contributions extracted near the base of the convection zone ($r/R_\odot = 0.74$). At this depth differential rotation is the primary contributor to the total mean flow. The turbulent EMF contribution (top panel) is seen to be spatiotemporally noisier than induction by the mean flow acting on the mean field (bottom panel). This was to be expected, since we are here taking spatial derivatives of a quantity, the turbulent EMF, which is itelf calculated from the large scale average of products of small scale, highly turbulent fields. Nonetheless, at any phase of the cycle both contributions are here clearly of the same overall order of magnitude. Furthermore, constructing similar diagrams at other depths indicate that this remains the case throughout the bulk of the convection zone. In the terminology of mean-field electrodynamics, one would then conclude that in this one specific simulation, the large-scale magnetic is sustained by an $\alpha^2\Omega$ dynamo.

3.2. Relating the α-tensor to kinetic and magnetic helicities

The mathematical machinery of mean-field electrodynamics goes well beyond the characterization of the turbulent EMF in terms of the mean magnetic field. In particular, for turbulent flows satisfying certain statistical properties and operating in certain specific physical regimes, it offers the mean of *calculating* the form of the α-tensor (see, e.g., Moffatt 1978). In the case of a turbulent flow that is isotropic and homogeneous but lacks reflectional symmetry, the α-tensor reduces to the diagonal form $\alpha\delta_{jk}$, with

$$\alpha = -\frac{\tau}{3} h_v \ , \tag{28}$$

where τ is the correlation time of the turbulence, and h_v is the mean kinetic helicity associated with this turbulent flow:

$$h_v = \langle \boldsymbol{u}' \cdot \nabla \times \boldsymbol{u}' \rangle \ . \tag{29}$$

The key result here is that albeit for the sign difference, the α-effect coefficient is directly proportional to the kinetic helicity, a quantity readily computed *a posteriori* from the simulation output. The result of such a calculation is plotted on Figure 8C, with the kinetic helicity having been averaged temporally as well as azimuthally over the complete time span of the simulation. Except for the sign difference, the degree of resemblance with the $\alpha_{\phi\phi}$ tensor component plotted on panel A is quite striking. Both functionals are strongly peaked at very high latitudes, and in each hemisphere only show a sign change near the base of the convection zone. The most prominent difference is found at low latitudes, where h_v shows a secondary peak in the middle of the convection zone that is absent in the $\alpha_{\phi\phi}$ profile. The $\alpha_{\theta\theta}$ component (see Fig. 7) is also tolerably well represented by the negative of the mean kinetic helicity, the most prominent discrepancy being that $\alpha_{\theta\theta}$ peaks at mid-latitudes. The α_{rr} diagonal component is that which shows the least similarity with the mean kinetic helicity, presumably because it is more sensitive to the break of homogeneity on which Eq. (28) is predicated, induced by stratification of the background state and/or upper boundary condition.

Equation (28) is predicated on a number of other strong assumptions, including the requirement that the small-scale turbulent flow remains entirely unaffected by the magnetic field. Once the magnetic field becomes dynamically significant, it is expected that it will alter the small-scale flow giving rise to the α-effect. Based on a set of local cartesian incompressible MHD simulations operating in the strongly nonlinear regime, Pouquet *et al.* (1976) suggested that Eq. (29) should be replaced by

$$\alpha = -\frac{\tau}{3} \left(h_v - h_B \right) \ , \tag{30}$$

where h_B is the mean current helicity, generalized to our anelastic MHD formulation as:

$$h_B = \frac{1}{\mu_0 \rho} \langle \boldsymbol{B}' \cdot \nabla \times \boldsymbol{B}' \rangle \ . \tag{31}$$

The physical link between kinetic and current helicity becomes more transparent upon noting that $\boldsymbol{B}'/\sqrt{\mu_0 \rho}$ is the Alfvén velocity, measuring the propagation speed of transverse MHD waves for

which magnetic tension provides the restoring force; what Eq. (30) expresses is simply that magnetic tension tends ot oppose any twisting of magnetic fieldlines by the small-scale turbulent flow. This quantity is plotted on Figure 8D, again as an azimuthal and temporal average spanning the full simulation duration. This magnetic contribution to the α-coefficient is found to be significantly smaller than its kinetic counterpart, by a factor of about ten. The strong peaks straddling the base of the convection zone at mid-latitude in both hemispheres are associated with the strong mean magnetic field building up in these regions, which, acted upon by the small-scale turbulent flow, feeds the production of small-scale current helicity.

The limited applicability of Eq. (30) to our simulation notwithstanding, the weak contribution of the specific current helicity as compared to the kinetic helicity term suggests that the dynamical impact of the small-scale magnetic component on the small-scale flow is correspondingly weak. Recall that we also demonstrated, in §2.6, that the α-tensor components does not show any significant variation with the strength of the large-scale magnetic component. This would suggest that the saturation of the dynamo amplitude must be achieved via a different mechanism, such as magnetic backreaction on the large-scale flow.

4. Discussion and conclusion

We have investigated the mode of large-scale dynamo action taking place in the global implicit large-eddy simulation of the solar convection zone reported upon in Ghizaru *et al.* (2010). Motivated by the presence of a strong and well-defined axisymmetric magnetic component arising in the simulation, we defined the large-scale magnetic field as the longitudinal average of the total simulated magnetic field, with the residual produced by subtracting this average component from the total field defining the small-scale, fluctuating magnetic component. Zonally averaging the cross-correlation of the latter with the corresponding small-scale flow component then allows the calculation of a turbulent electromotive force, and its development in terms of the large-scale, zonally-averaged component allows to calculate the components of the α-tensor. The α-tensor components so calculated were found to compare well to a number of results obtained in local cartesian simulations with an externally imposed large-scale magnetic component. Noteworthy results include: a positive $\alpha_{\phi\phi}$ component in the Northern solar hemisphere, peaking at high latitude and changing sign near the base of the convecting shell; downward turbulent pumping in the bulk of the convection zone, except in a thin subsurface layer where pumping is upward-directed; significant latitudinal pumping, equatorward at mid- to low-latitude in the bulk of the convecting layer, but poleward in the high-latitude, subsurface layers.

Because our simulation generates its own large-scale magnetic field, no such field need be imposed externally to measure the α-effect. The α-effect that we do measure is then dynamically consistent with the nonlinear interaction of flow and field at all numerically resolved spatial and temporal scales. However, our results are physically meaningful only to the degree that the scale separation procedure used to divide the total flow and field into mean and fluctuating components

is applicable to our simulation results. The modal analysis described in §2.1 suggests that it is. Moreover, Figure 9 provides additional empirical evidence that something closely akin to the α-effect of mean-field electrodynamics offers an adequate representation of the turbulent electromotive force arising in the simulation.

The mean-field analysis reported upon in this paper relies entirely on *a posteriori* calculations of cross-correlations between the small-scale flow and magnetic field, as defined via Eqs. (4)–(5) *and as resolved by our computational grid*. The implicit presence of dissipative terms at the level of the MPDATA advection scheme at the core of EULAG has been shown, in the context of purely hydrodynamical simulations, to mimic subgrid dynamical processes such as self-similar energy cascade (Domaradzki *et al.* 2003; Margolin *et al.* 2006; Margolin & Rider 2007). Evidently, the smallest resolved scales in our simulation have been influenced by these subgrid effects, and therefore so has our reconstructed EMF; yet the overall dynamo picture emerging from our analysis shows remarkable internal self-consistency, which suggests that MHD subgrid effects, if present, are not the primary direct drivers of cyclic evolution on large spatial scales.

The simultaneous presence of globally well-structured α-effect and significant internal differential rotation suggests that our simulation could be operating as what is known in mean-field electrodynamics as an $\alpha\Omega$ dynamo. This inference is buttressed by a number of simulation features, notably the fact that the in-phase (or nearly so) production of a positive large-scale dipole moment from a positive toroidal component is what is expected of kinematic $\alpha\Omega$ dynamo models having the angular velocity outwardly increasing on cylindrical isocontours and $\alpha_{\phi\phi} > 0$ in the Northern solar hemisphere (see Stix 1976). Oscillatory behavior has been shown to be possible also in linear α^2-type models, i.e., in the complete absence of differential rotation, provided the α-effect has sufficiently steep radial variations, including sign changes (Stefani & Gerbeth 2003). Such oscillatory α^2-type solutions were recently identified in the helically-forced MHD simulations of Mitra *et al.* (2010). These authors also presented specific examples showing that such externally-forced α^2 dynamo models could also exhibit latitudinal propagation of the azimuthal large-scale magnetic component. Given the rather complex spatial variations of our measured α-tensor components (see Fig. 7), it then remains possible that the α-effect is the primary driver of the polarity reversals and mild equatorward propagation of the deep-seated mean magnetic component observed in our simulation. Then again, the comparable magnitudes of the small-scale and large-scale contributions to the ϕ-component of the induction term (cf. Fig. 12A and B) would rather point to the so-called $\alpha^2\Omega$ dynamo, in which shearing by the large-scale flow and the turbulent EMF both contribute to the regeneration of the large-scale toroidal magnetic component. Unless differential rotation is very weak, such dynamos behave qualitatively like $\alpha\Omega$ dynamos. In particular, they also support travelling dynamo waves propagating according to the Parker-Yoshimura sign rule (see, e.g., Choudhuri 1990; Charbonneau & MacGregor 2001). At a given turbulent intensity, the distinction between these three classes of models therefore hinges on the magnitude of differential rotation in the region where dynamo action is taking place.

Interestingly, the pole-to-equator angular velocity contrast in a purely hydrodynamical simu-

lation using the same stratification and thermal forcing as in Ghizaru *et al.* (2010) is much closer to solar, indicating that the magnetic field —both small-scale and large-scale— has a significant impact on the dynamics of large-scale flow building up in the simulation. A similar behavior was observed already in the simulations of Gilman (1983), and carried over also to the simulations of Browning *et al.* (2006). Assume for the sake of the discussion that a stronger, solar-like internal differential rotation could be produced in our simulation, e.g., by introducing a latitudinal gradient in the thermal forcing, as done in Miesch *et al.* (2006) and Browning *et al.* (2006). In kinematic $\alpha\Omega$ mean-field models operating close to criticality, the cycle frequency is found to increase as a power, usually close to unity, of the so-called dynamo number D, defined as

$$D = \frac{\alpha_0(\Delta\Omega)R^3}{\eta_T^2} \ , \tag{32}$$

where R is a measure of the size of the dynamo region (often taken as the solar/stellar radius), α_0 measures the magnitude of the α-effect, $\Delta\Omega$ that of the differential rotation, and η_T is the turbulent diffusivity value used in the model. Consider now our simulation; assuming that ramping up $\Delta\Omega$ by a factor of three can be achieved without affecting too much the EMF or turbulent diffusivity, Eq. (32) would then predict a decrease of the cycle period by a factor of ~ 3, which would bring it down to the solar value. This would alleviate simultaneously two of the primary failings of the present simulation as compared to the solar cycle, namely the latitudinal surface differential rotation being too weak, and the cycle period being too long. On the other hand, the fact that the large-scale poloidal and toroidal components oscillate almost exactly in phase, may well lie outside the reach of these types of global MHD simulations. Modelling of the solar surface magnetic flux evolution (e.g. Wang & Sheeley 1991; Schrijver *et al.* 2002; Baumann *et al.* 2004) has shown that the poleward transport of magnetic decay products of sunspots and active regions by supergranular diffusion and the poleward meridional flow is an important driver of polar field reversals. There is of course nothing equivalent to decaying active regions in our simulations, so in retrospect an incorrect timing of surface polar field reversals is perhaps not exceedingly worrisome.

The question of cycle amplitude saturation also merits further investigation. The analysis of §2.6 already suggests that nothing akin to classical α-quenching by the mean magnetic field is taking place in the simulation, and that of §3.2 suggests that quenching by the small-scale magnetic component is also insignificant. Further insight can be gained by examining the relative contributions of the small- and large-scale flow and magnetic field to the global specific energy budget. We simply define these contributions as volume averages over the full simulation domain:

$$E(\langle u\rangle) = \frac{1}{2}\int_V \langle u\rangle^2 \mathrm{d}V \ , \tag{33}$$

$$E(u') = \frac{1}{2}\int_V (u')^2 \mathrm{d}V \ , \tag{34}$$

$$E(\langle B\rangle) = \frac{1}{\mu_0}\int_V \rho^{-1}\langle B\rangle^2 \mathrm{d}V \ , \tag{35}$$

$$E(B') = \frac{1}{\mu_0} \int_V \rho^{-1} (B')^2 \mathrm{d}V \ , \tag{36}$$

with $\langle u \rangle^2 = \langle \boldsymbol{u} \rangle \cdot \langle \boldsymbol{u} \rangle$, etc. The comparison between these various contributions is carried out pictorially on Fig. 13, in the form of time series spanning the full simulation run. The cycle stands out as a prominent cyclic variation in the energy contribution of the large-scale magnetic field, which varies by a factor 2—3 between epochs of cycle "maxima" and "minima". Interestingly, the energy contributions of the small-scale flow remain remarkably steady in comparison. Recall that the requirement for $\boldsymbol{u'}$ to be independent of $\langle \boldsymbol{B} \rangle$ was in fact a sine qua non condition for Eq. (9) to be physically meaningful. Even though it is defined globally, the steadiness of the $E(u')$ time series is consistent with the conclusion already drawn on the basis of Fig. 11, namely that the α-tensor is not affected by the presence of the large-scale magnetic field. In contrast, the small-scale magnetic energy $E(B')$ does show some in-phase variations with $E(\langle B \rangle)$, which probably indicates that our scale separation breaks down at some level. Detailed examination of the modal decomposition indicates that this occurs primarily below the core-envelope interface, and therefore the impact on the calculation of the turbulent EMF and α-tensor component in all likelihood remains small.

Things become more interesting with the kinetic energy associated with the large-scale flow, which does show a clear cyclic variation, approximately in anti-phase with the large-scale magnetic energy for most cycles; this suggests that dynamo saturation takes place via magnetic backreaction on the large-scale flow. This inference also finds support in the fact that the overall level of differential rotation in the simulation, as measured, e.g., by the pole-to-equator angular velocity contrast, is smaller by a factor of three than the same constrast materializing in an unmagnetized, purely hydrodynamical version of the simulation under the same forcing parameters. It remains to be investigated whether magnetic backreaction on the large-scale flow is mediated by the Lorentz force component associated with the large-scale magnetic field (the so-called Malkus-Proctor effect), or through small-scale Maxwell stresses, either directly or through quenching of the small-scale Reynolds stresses powering the large-scale flow (sometimes refered to as Λ-quenching; see, e.g., Kitchatinov & Rüdiger 1993; Rempel 2006; and references therein).

Another intriguing question relates to the mechanism(s) responsible for the equatorward propagation of the sunspot activity belts in the course of the cycle. If sunspots are assumed to originate from the destabilisation and vertical rise of toroidal magnetic flux ropes stored immediately beneath the solar core-envelope interface, then the observed equatorward drift should reflect a similar drift in the deep-seated toroidal magnetic components from which these flux ropes are believed to form. The weak equatorial propagation visible on the top panel of Fig. 2 amounts to a drift speed in the range 0.3–0.5 m s^{-1}, while in the sun this speed is estimated at 1 m s^{-1}. In the simulation considered here, a weak positive radial differential rotation is sustained at mid to low-latitudes at the core-envelope interface. In conjunction with a negative $\alpha_{\phi\phi}$ at the base of the envelope (see Fig. 7, bottom right meridional slice), we then have $\alpha_{\phi\phi} \times \mathrm{d}\Omega/\mathrm{d}r < 0$, which should then lead to equatorward propagation of the dynamo wave as per the Parker-Yoshimura sign rule. Then again, our simulation is also characterized by a mean meridional flow component which, at mid-latitude at the core-envelope interface, is equatorward and reaches a few tenths of meters per second, compa-

rable to the drift speed infered from Fig. 2. Moreover, as discussed in §2.5 the latitudinal turbulent pumping at the base of the envelope is equatorward and also reaches a few tenths of meters per second. Because the large-scale differential rotation and meridional flow both show significant temporal variations in phase with the cycle of the large-scale magnetic field, deciding whether it is the large-scale flows that drive the magnetic cycle, of the magnetic field that propels the flows, again requires a complete and detailed investigation of the dynamical balance arising in the simulation. Such an analysis is now underway, and will be reported upon in a future paper.

We wish to thank Patrice Beaudoin for assistance in the preparation of the final version of Figure 8. The numerical simulations reported upon in this paper were carried out primarily on the computing facilities of the Réseau Québécois de Calcul de Haute Performance. This work is supported by Canada's Natural Sciences and Engineering Research Council, Research Chair Program, and Foundation for Innovation (ER, PC, MG and AB). The National Center for Atmospheric Research is sponsored by the National Science Foundation (PKS).

REFERENCES

Baumann, I., Schmitt, D., Schüssler, M., & Solanki, S, 2004, A&A, 426, 1075

Brandenburg, A. 2009, SSRv, 144, 87

Browning, M.K., Miesch, M.S., Brun, A.S., & Toomre, J. 2006, ApJ, 648, L157

Brown, B.P., Browning, M.K., Brun, A.S., Miesch, M.S., & Toomre, J. 2010a, ApJ, 711, 424

Brown, B.P., Miesch, M.S., Browning, M.K., Brun, A.S., & Toomre, J. 2010b, submitted to ApJ

Brun, A.S., Miesch, M.S., & Toomre, J. 2004, ApJ, 614, 1073

Cattaneo, F., & Hughes, D.W. 2009, MNRAS, 395, L48

Charbonneau, P. 2010, LRSP, 7, lrsp-2010-3

Charbonneau, P., & MacGregor, K.B. 2001, ApJ, 559, 1094

Choudhuri, A.R. 1990, ApJ, 355, 733

Christensen-Dalsgaard, J. 2002, RMP, 74, 1073

Clune, T.L., Elliot, J.R., Glatzmaier, G.A., Miesch, M.S., & Toomre, J., 1999, Parallel Comput., 25, 361

Davidson, P.A. 2001, *An Introduction to Magnetohydrodynamics*, Cambridge: Cambridge University Press

Domaradzki, A., Xiao, Z, Smolarkiewicz, P.K., 2003, Phys. Fluids, 15, 3890

Elliott, J.R., & P.K. Smolarkiewicz, P.K. 2002, Int. J. Numer. Meth. Fluids, 39, 855

Fan, Y. 2009, LRSP, 6, lrsp-2009-4

Ferriz-Mas, A., Schmitt, D., & Schüssler, M. 1994, A&A, 289, 949

Ghizaru, M., Charbonneau, P., & Smolarkiewicz, P.K. 2010, ApJL, 715, L133

Gilman, P. 1983, ApJS, 53, 243

Glatzmaier, G.A. 1984, J. Comput. Phys., 55, 461

Glatzmaier, G.A. 1985, ApJ, 291, 300

Goedbloed, H., & Poedts, S. 2004, *Principles of Magnetohydrodynamics*, Cambridge: Cambridge University Press

Hathaway, D.H. 2010, LRSP, 7, lrsp-2010-1

Held, I.M., & Suarez, M.J. 1994, Bull. Amer. Meteor. Soc., 75, 1825

Hoyng, P. 2003, in *Advances in nonlinear dynamos*, eds. A. Ferriz-Mas & M. Núñez, London: Taylor & Francis, 1-36

Hubbard, A., DelSordo, F., Käpylä, P.J., & Brandenburg, A. 2009, MNRAS, 398, 1981

Käpylä, P.J., Korpi, M.J., Ossendrijver, M., & Stix, M. 2006, A&A, 455, 401

Käpylä, P.J., Korpi, M.J., & Brandenburg, A. 2009, A&A, 500, 633

Käpylä, P.J., Korpi, M.J., Brandenburg, A., Mitra, D., & Tavakol, R. 2010, AN, 331, 73

Kitchatinov, L.L., & Rüdiger, G. 1993, ApJ, 276, 96

Krause, F., & Rädler, K.-H. 1980, *Mean-Field Magnetohydrodynamics and Dynamo Theory*, Oxford: Pergamon Press

Margolin, L. G., Rider, W. J. & Grinstein, F.F. 2006, J. Turb., 7, N15

Margolin, L. G., Rider, W. J. 2007, in *Implicit Large Eddy Simulation: Computing Turbulent Fluid Dynamics*, eds. F F. Grinstein, L.G. Margolin & W.J. Rider, Cambridge: Cambridge University Press, 195-221

Miesch, M.S., Brun, A.S., & Toomre, J., 2006, ApJ, 641, 618

Miesch, M.S., Brown, B.P., Browning, M.K., Brun, A.S., & Toomre, J., 2011, in *From Stars to Galaxies*, IAU Symp., eds. N. Brummell, A.S. Brun & M.S. Miesch, in press

Miesch, M.S., & Toomre, J., 2009, Ann. Rev. Fluid Mech., 41, 317

Mitra, D., Tavakol, R., Käpylä, P.J., & Brandenburg, A. 2010, ApJL, 719, L1

Moffatt, H.K. 1978, *Magnetic field generation in electrically conducting fluids*, New York: Cambridge University Press

Ossendrijver, M.A.J.H. 2003, A&AR, 11, 287

Ossendrijver, M.A.J.H., Stix, M., Brandenburg, A., & Rüdiger, G. 2002, A&A, 394, 735

Ossendrijver, M.A.J.H., Stix, M., & Brandenburg, A. 2001, A&A, 376, 731

Parker, E.N. 1955, ApJ, 122, 293

Piotrowski, Z.P., Smolarkiewicz, P.K., Malinowski, S.P., & Wyszogrodzki, A.A. 2009, J. Comput. Phys, 228, 6268

Pouquet, A., Frisch, U., & Leorat, J. 1976, JFM, 77, 321

Press, W.H., Teukolsky, S.A., Vetterling, W.T., & Flannery, B.P. 1992, *Numerical Recipes in C*, 2$^{\rm nd}$ed., Cambridge University Press

Prusa, J.M., Smolarkiewicz, P.K., & Wyszogrodzki, A.A. 2008, Comp. Fluids, 37, 1193

Rempel, M. 2006, ApJ, 647, 662

Rüdiger, G., & Kitchatinov, L.L. 1993, A&A, 269, 581

Rüdiger, G., & Hollerbach, R. 2004, *The magnetic universe*, Wiley-Interscience

Schrijver, C.J., DeRosa, M.L., & Title, A.M., ApJ, 577, 1006

Smolarkiewicz, P.K. 2006, Int. J. Numer. Methods Fluids, 50, 1123

Smolarkiewicz, P.K., Margolin, L.G., & Wyszogrodzki, A. A. 2001, J. Atmos. Sci., 58, 349

Smolarkiewicz, P.K., & Szmelter, J. 2009, J. Comput. Phys., 228, 33

Stefani, F., & Gerberth, G. 2003, PRE, 67, 027302

Stix, M. 1976, A&A, 47, 243

Wang, Y.-M., & Sheeley, N.R.Jr. 1991, ApJ, 375, 761

This preprint was prepared with the AAS LaTeX macros v5.2.

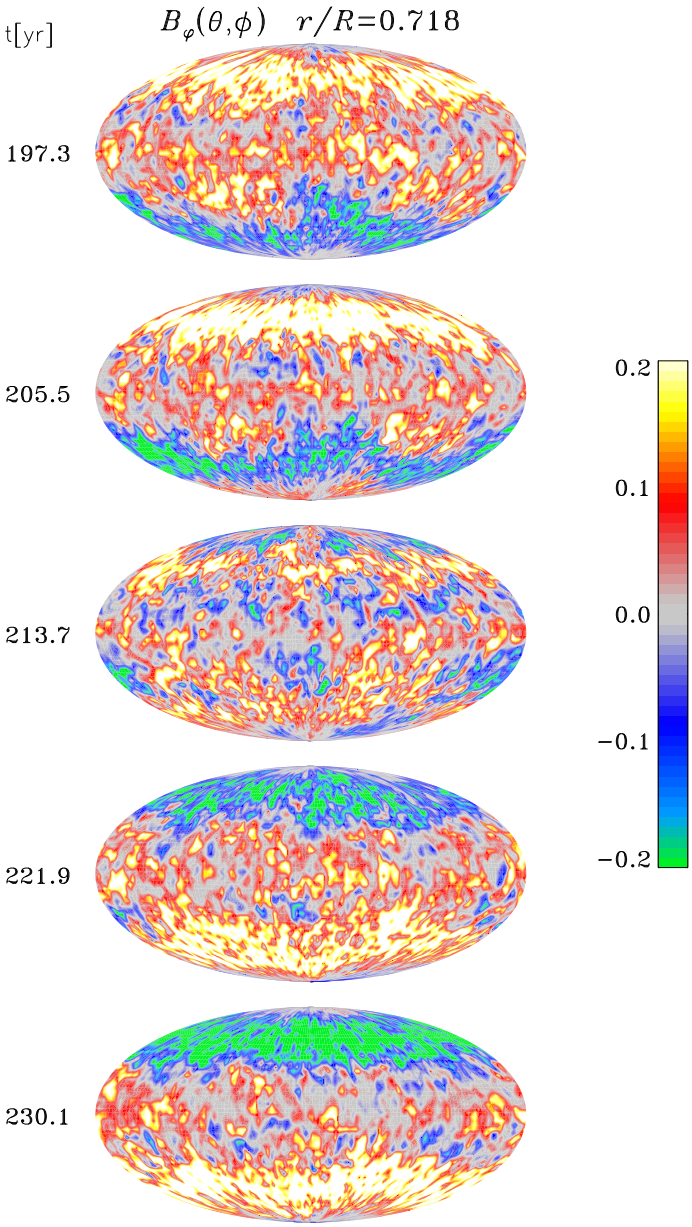

Fig. 1.— Temporal sequence of the toroidal magnetic component extracted at the core-envelope interface ($r/R_\odot = 0.718$) in the 3D MHD simulation presented in Ghizaru *et al.* (2010), plotted in Mollweide projection. The sequence runs from top to bottom, and covers a time interval corresponding to a half-cycle, temporally centered on a polarity reversal. The color scale codes the magnetic field strength, in Tesla. [We will make this available as an animation supplement for the online version]

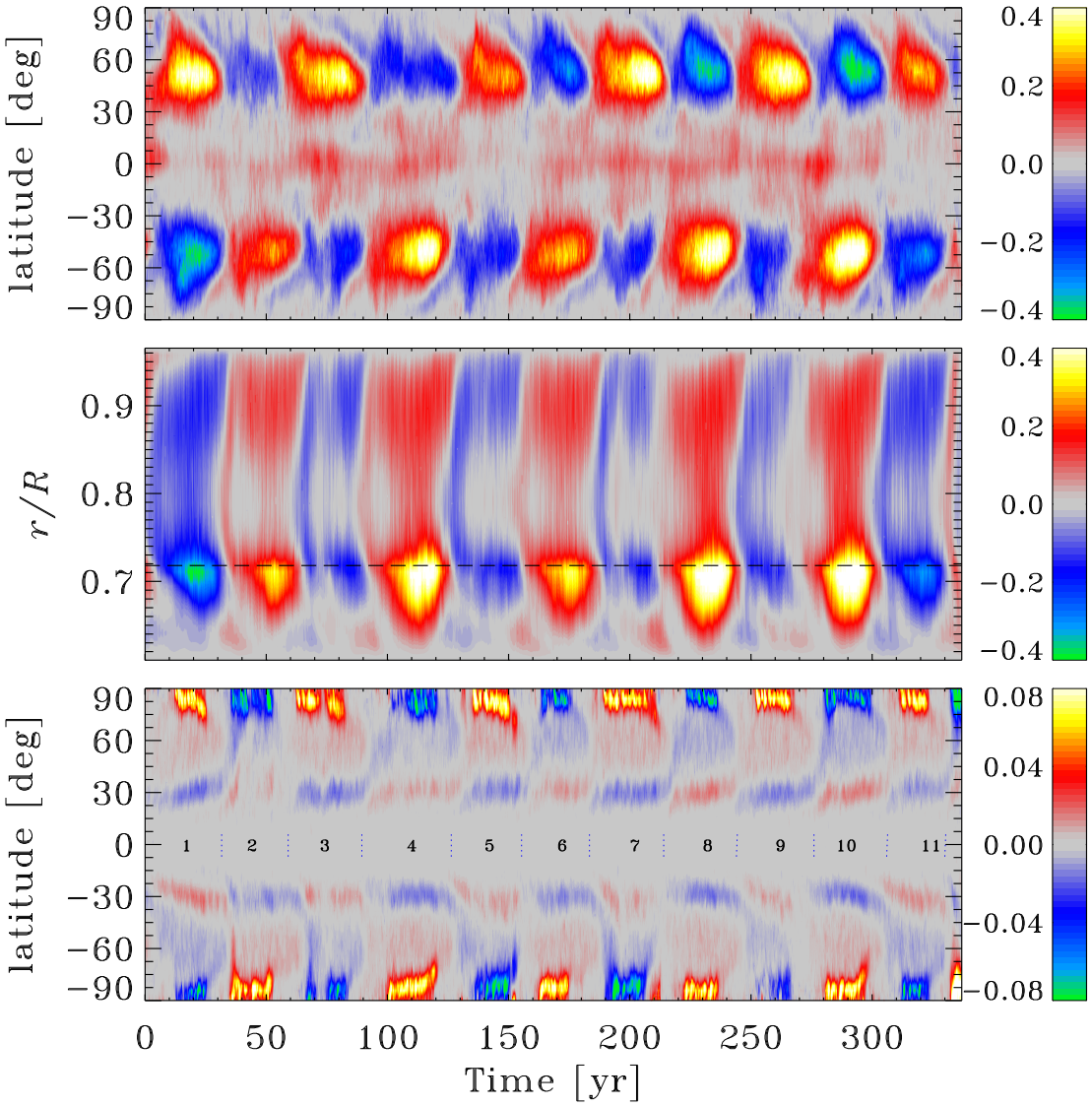

Fig. 2.— Spatiotemporal evolution of the zonally-averaged magnetic field in the 3D MHD simulation of Ghizaru *et al.* (2010). Top panel: time-latitude diagram of the zonally-averaged toroidal magnetic component at the core-envelope interface ($r/R_\odot = 0.718$); middle panel: corresponding radius-latitude diagram, extracted at latitude $-45°$ in the southern hemisphere. The dashed line indicates the core-envelope interface; bottom panel: time-latitude diagram of the zonally-averaged surface radial field ($r/R_\odot = 0.96$), with magnetic half-cycles numbered from minima ot minima, as with the sunspot cycles. The color scale codes the magnetic field strength, in Tesla.

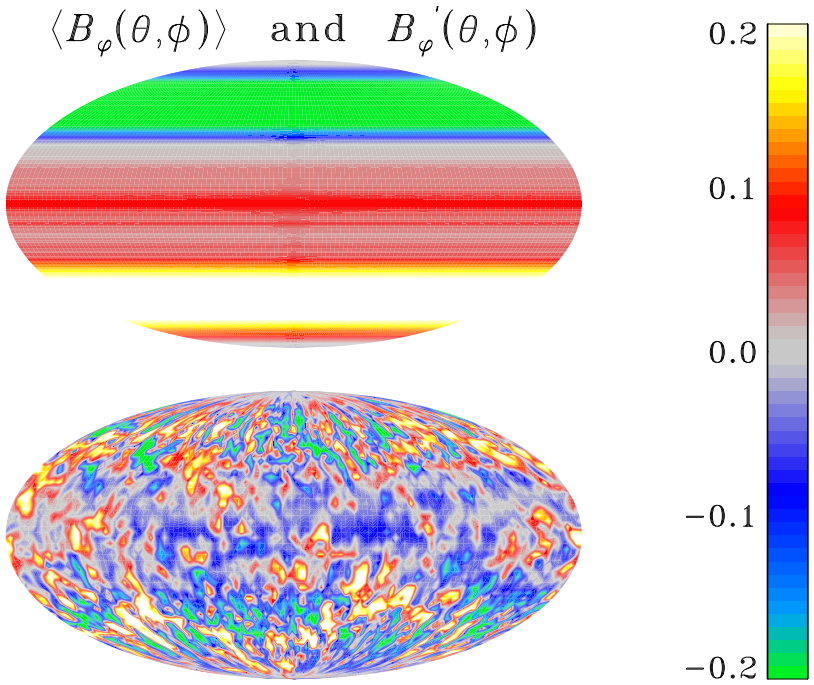

Fig. 3.— Latitude-longitude Mollweide projection of the zonally averaged toroidal magnetic component (top), and associated small-scale fluctuating toroidal component (bottom), as defined by Eq. (5), extracted at a depth corresponding to the core-envelope interface at simulation time $t = 230$, near the peak of magnetic half-cycle number 8 (see Figure 2). The sum of these two components is the total toroidal field distribution plotted on the bottom panel of Fig. 1.

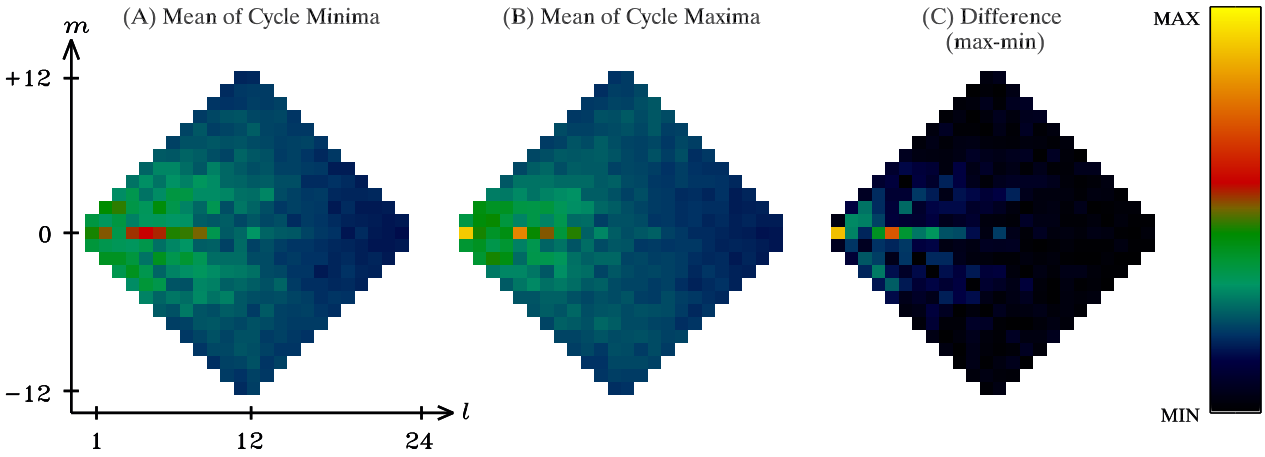

Fig. 4.— Spectral distribution of modal amplitudes for the toroidal magnetic component at the core-envelope interface in the simulation, $r/R_\odot = 0.718$. The unsigned values resulting from a standard spherical harmonic decomposition were averaged over two set of disjointed blocks centered over cycle minima (panel A) and maxima (panel B), respectively. Panel C results from subtracting panel A from panel B, and shows the amplitude distribution associated with the large-scale magnetic component, which is concentrated primarily in the $(\ell, m) = (1, 0)$ and $(5, 0)$ modes. The color scale spans two orders of magnitude, in constant logarithmic increments.

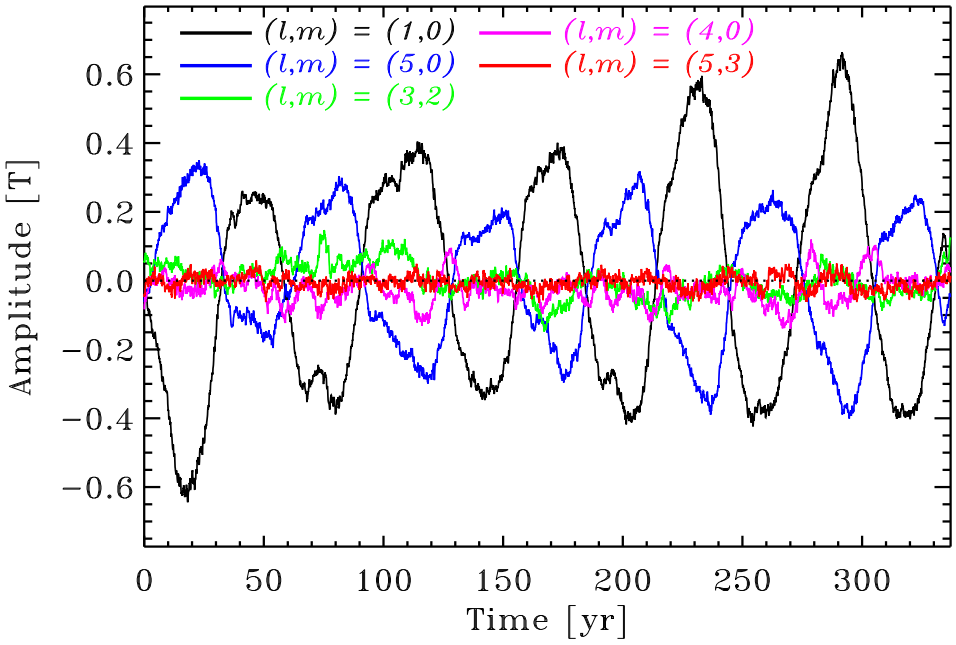

Fig. 5.— Time series of a few selected spherical harmonic coefficients, as labeled, over the full simulation run. While the cycle shows up prominently in axisymmetric ($m = 0$) modes of low, odd angular degree ℓ, at high wavenumber the time series show no clear cyclic variations.

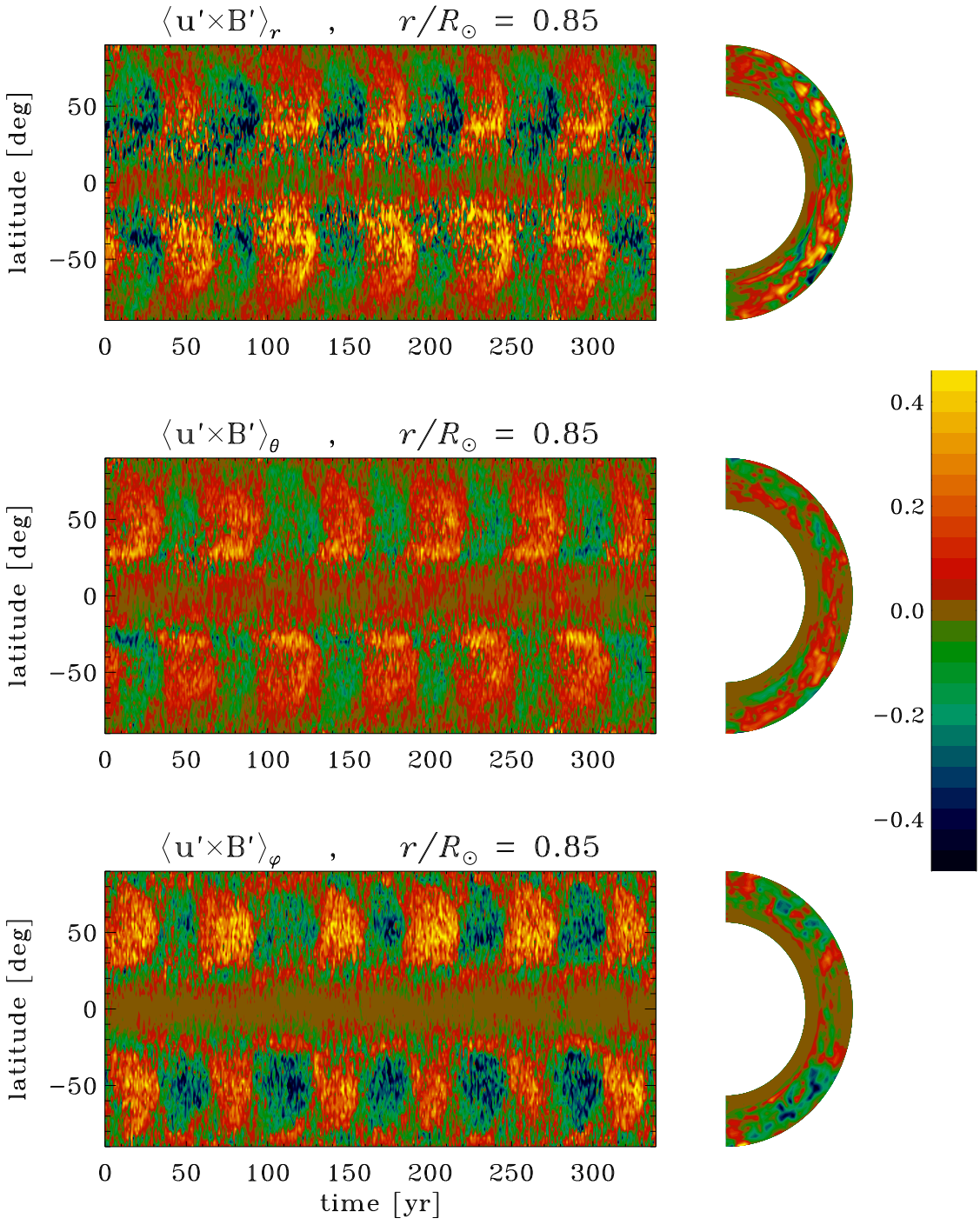

Fig. 6.— The three components of the turbulent EMF $\langle \boldsymbol{u}' \times \boldsymbol{B}' \rangle$. The left column shows time-latitude slices extracted at the middle of the convection zone (depth $\sim r/R_\odot = 0.85$), while the right column shows snapshots of the spatial variations in meridional planes, at the peak of simulate cycle 4. For the purpose of constructing the time-latitude diagrams, the simulation was undersampled at intervals of 10 solar days ($\simeq 0.82\,\mathrm{yr}$).

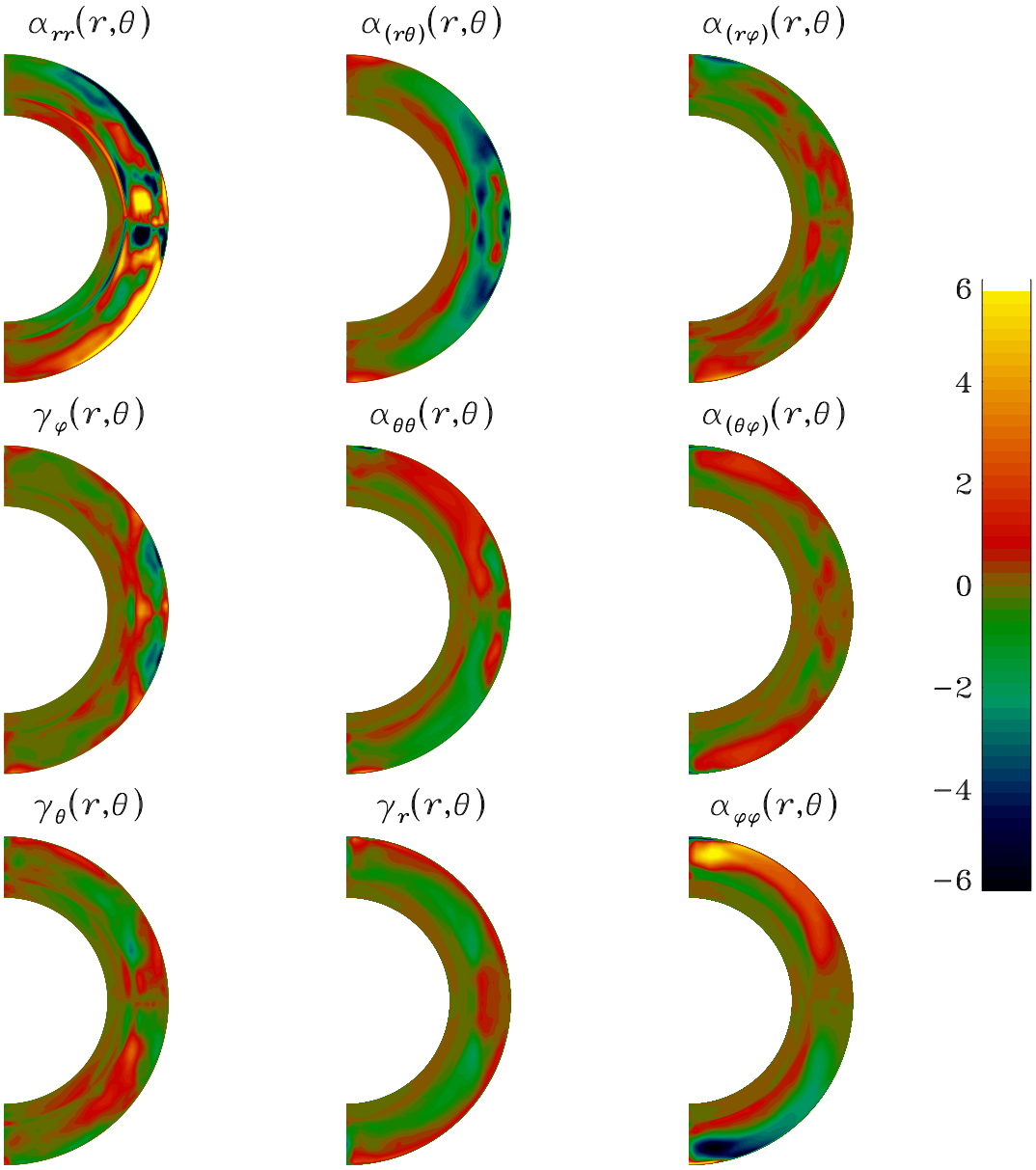

Fig. 7.— The components of the α-tensor, plotted in meridional plane. The color scale encodes the magnitude, in m s^{-1}, and is the same for all plots. The three plots along the diagonal correspond to α_{rr}, $\alpha_{\theta\theta}$, and $\alpha_{\phi\phi}$; the three plots above the diagonal to the corresponding off-diagonal component of the symetric part of the tensor, and the three plots below the diagonal to the three components of the turbulent pumping velocity, as labeled and directly related to the three non-zero component of the antisymmetric part of the full α-tensor via Eq. (12). The fitting procedure treats each hemisphere separately, so that the high degree of symmetry or antisymmetry about the equatorial plane characterizing the various tensor components is not a fitting artefact.

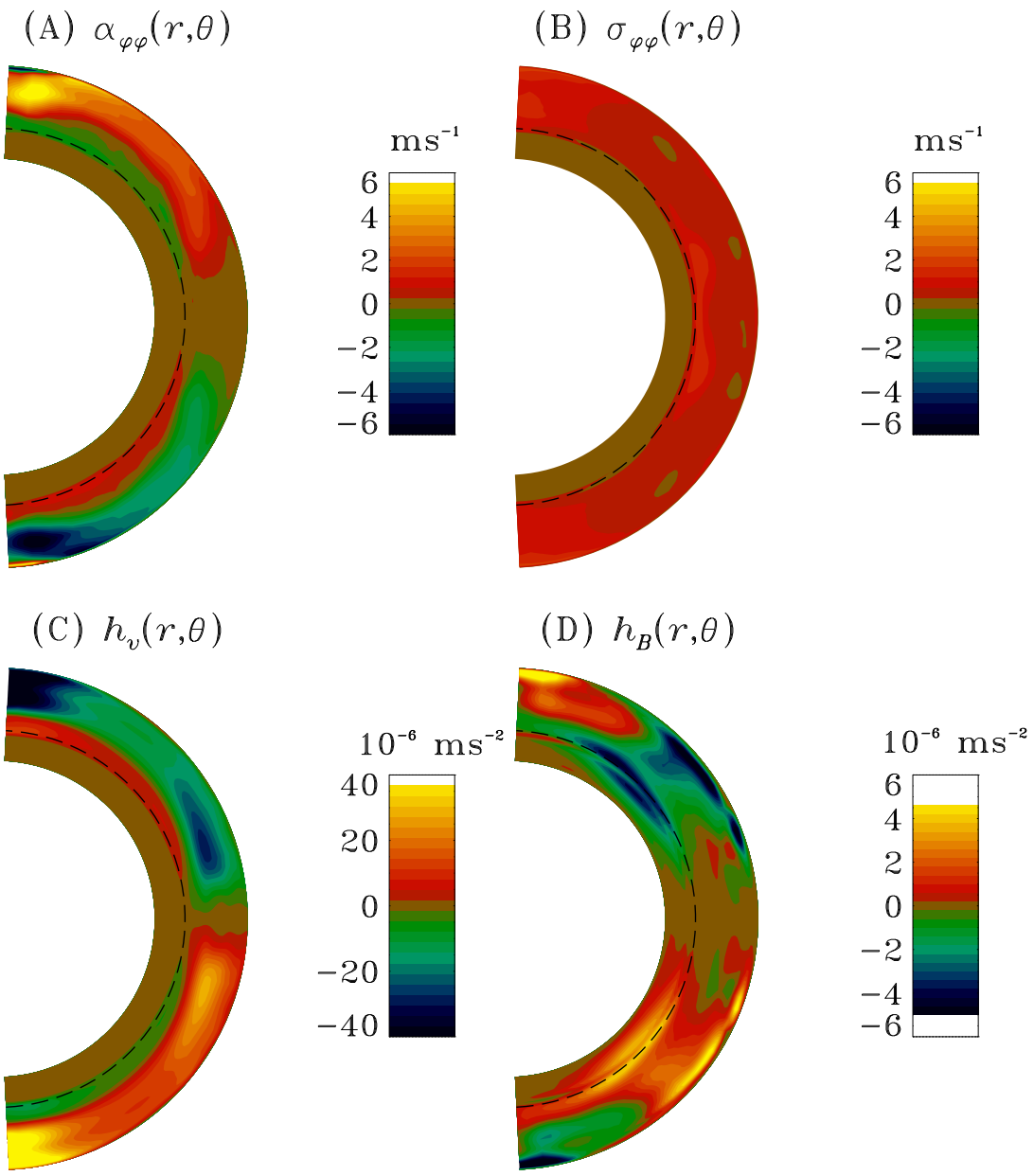

Fig. 8.— Meridional slice plots of (A) $\alpha_{\phi\phi}$, replotted directly from Figure 7; (B) its standard deviation as returned by the fitting procedure based on singular value decomposition, purposefully plotted using the same color scale as in A even though negative values are here meaningless. The variance is artificially set to zero below the core-envelope interface; (C) temporally- and zonally-averaged kinetic helicity; (D) temporally- and zonally-averaged specific current helicity. The dashed circular arc indicates the core-envelope interface.

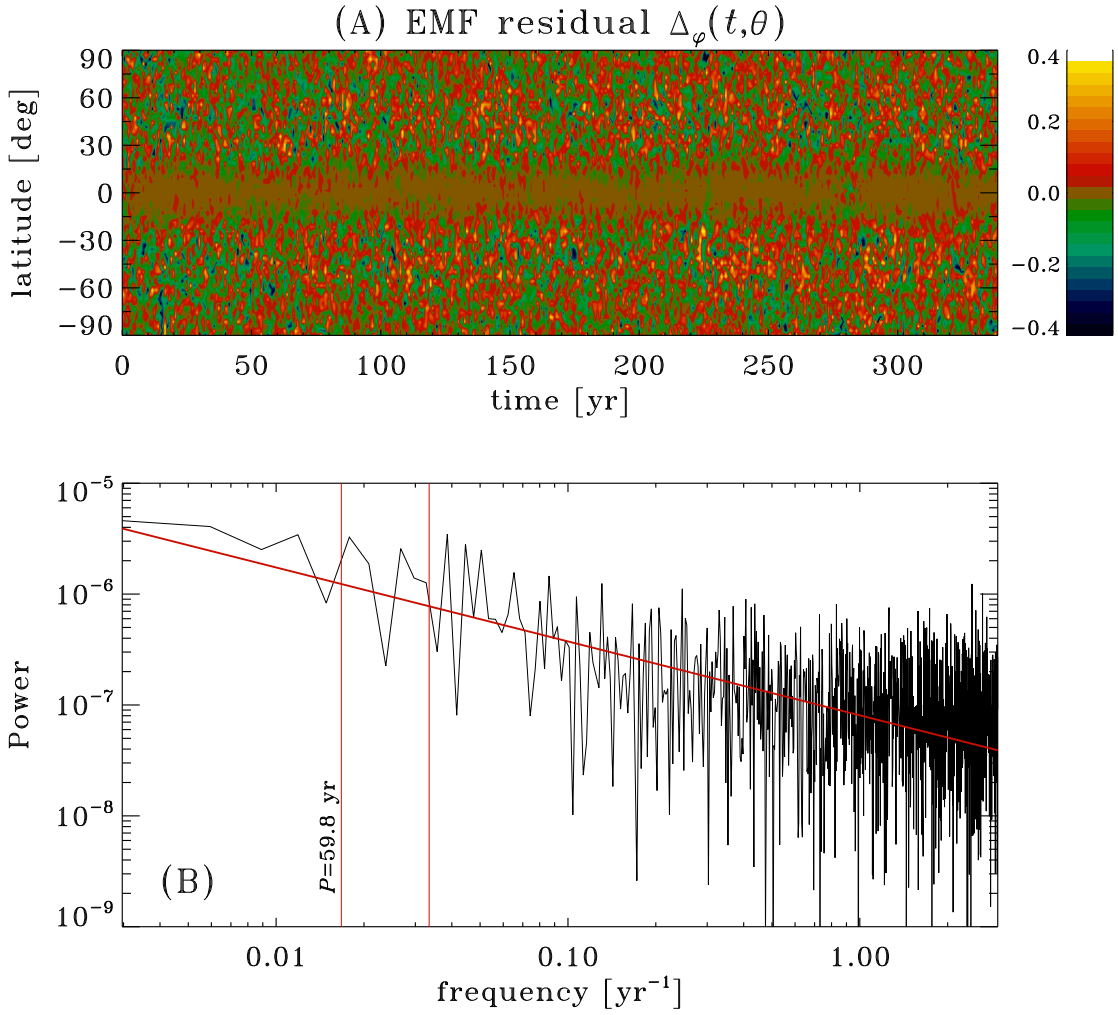

Fig. 9.— (A) Time latitude diagram of the EMF residual defined by Eq. (21), constructed on a sphere of radius $r/R_\odot = 0.8$. (B) Power spectrum of the residuals of part (A) now averaged in latitude to produce a simple time series. The sloping red line is a guide to the eye, showing a power-law spectrum with logarithmic slope $-2/3$. The vertical line segment originating from the abcissa indicate the frequencies corresponding to the primary magnetic cycle (full period 59.8 yr), and its first few harmonics.

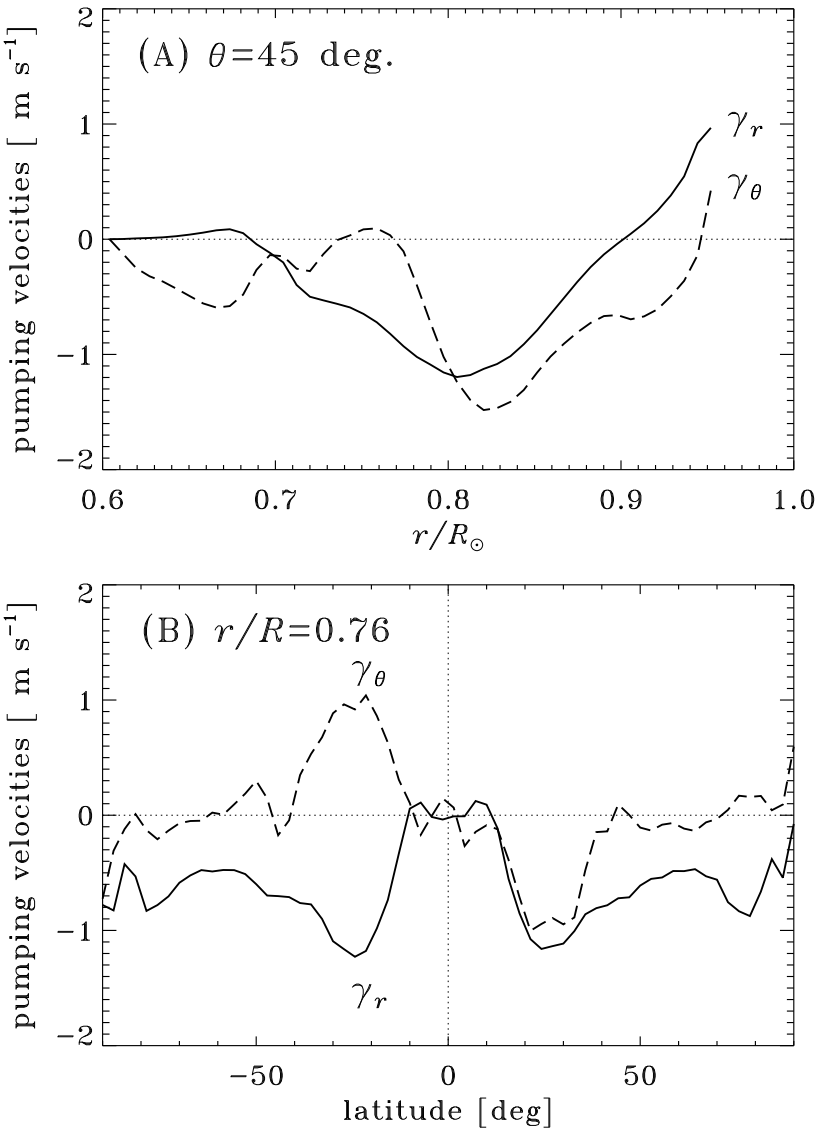

Fig. 10.— (A) Radial and (B) latitudinal cuts of the radial (solid lines) and latitudinal (dashed lines) turbulent pumping velocity components, extracted at latitude 45° in (A), and at depth $r/R_\odot = 0.76$ in (B). Radial pumping is downward in the bulk of the convecting layers, except near the surface, while latitudinal pumping is equatorward at mid to low latitudes. See also the bottom-left (γ_θ) and and bottom-middle (γ_r) panels on Fig. 7.

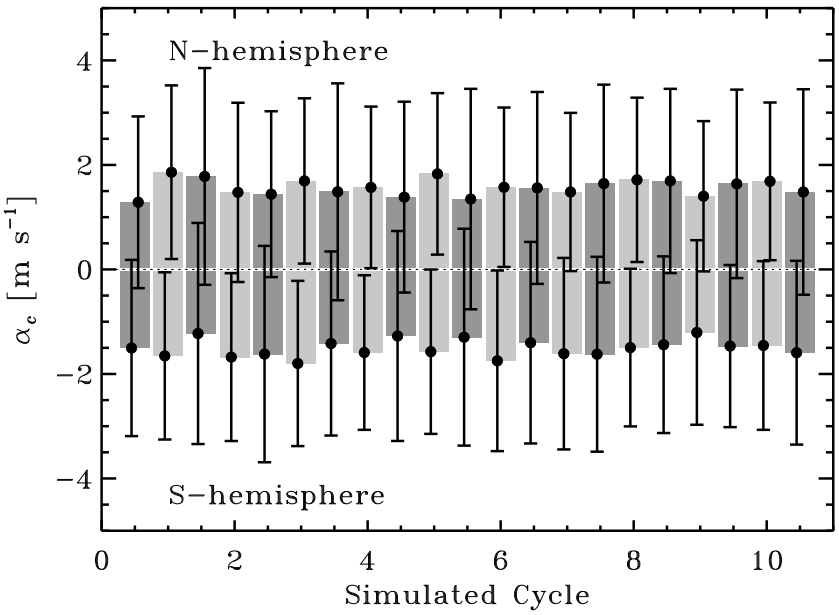

Fig. 11.— Temporal variation of the spatially-averaged $\alpha_{\phi\phi}$ tensor component, computed separately in each hemisphere according to Eq. (23b); this yields positive (negative) values in the Northern (Southern) solar hemisphere. The darker shading corresponds to blocks centered on times of maxima in $\langle \boldsymbol{B} \rangle$, and the lighter shades to interleaved blocks centered on times of polarity reversals. The error bars are computed from the variance returned by the SVD fitting algorithm, via Eq. (20). Qualitatively similar results are obtained for other α-tensor components, i.e., no significant variation between epochs of cycle maxima and minima.

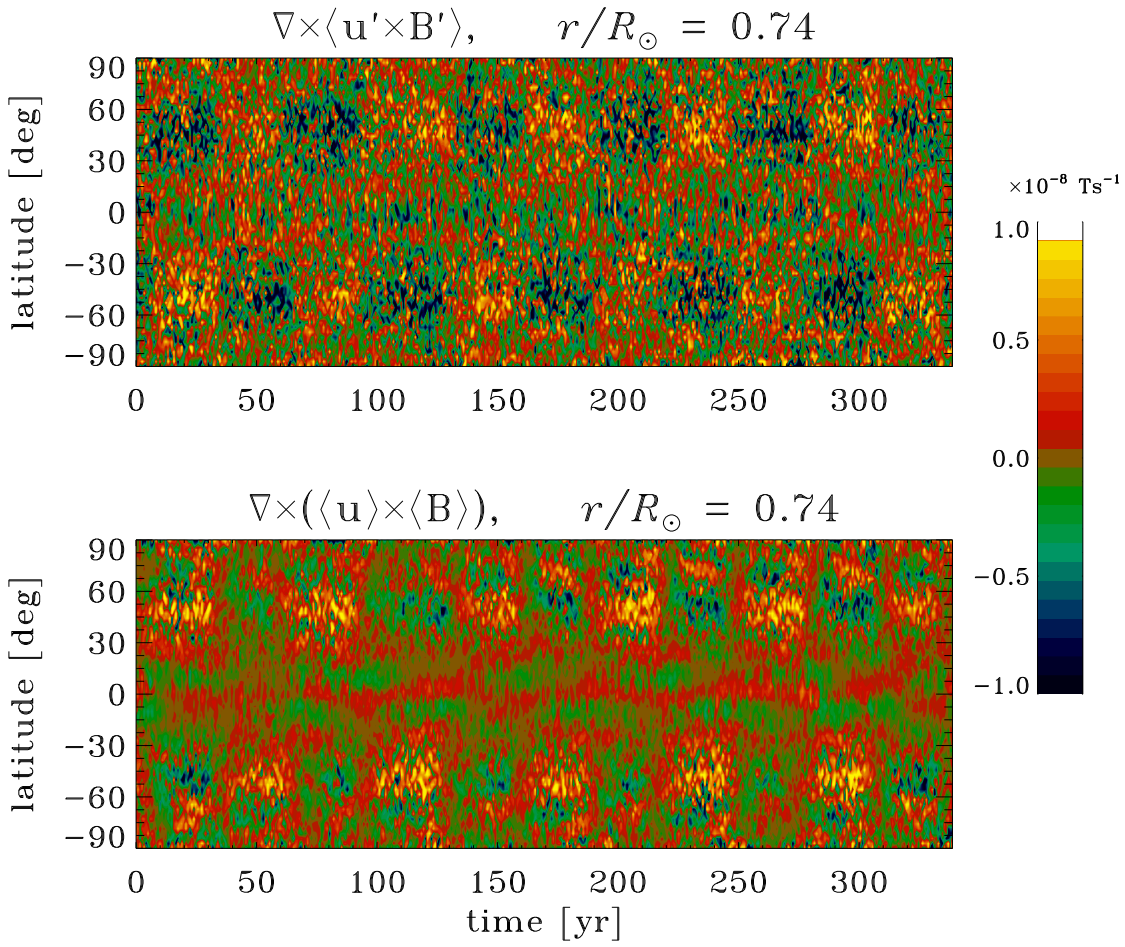

Fig. 12.— Time-latitude diagrams for the azimuthal components of the inductive contributions $\nabla \times \langle \boldsymbol{u}' \times \boldsymbol{B}' \rangle$ (top panel) and $\nabla \times (\langle \boldsymbol{u} \rangle \times \langle \boldsymbol{B} \rangle)$ (bottom panel), constructed at depth $r/R_\odot = 0.74$, near base of the convection zone. Although the contribution of the turbulent EMF is spatiotemporally noisier, both contributions are here roughly of the same order of magnitude.

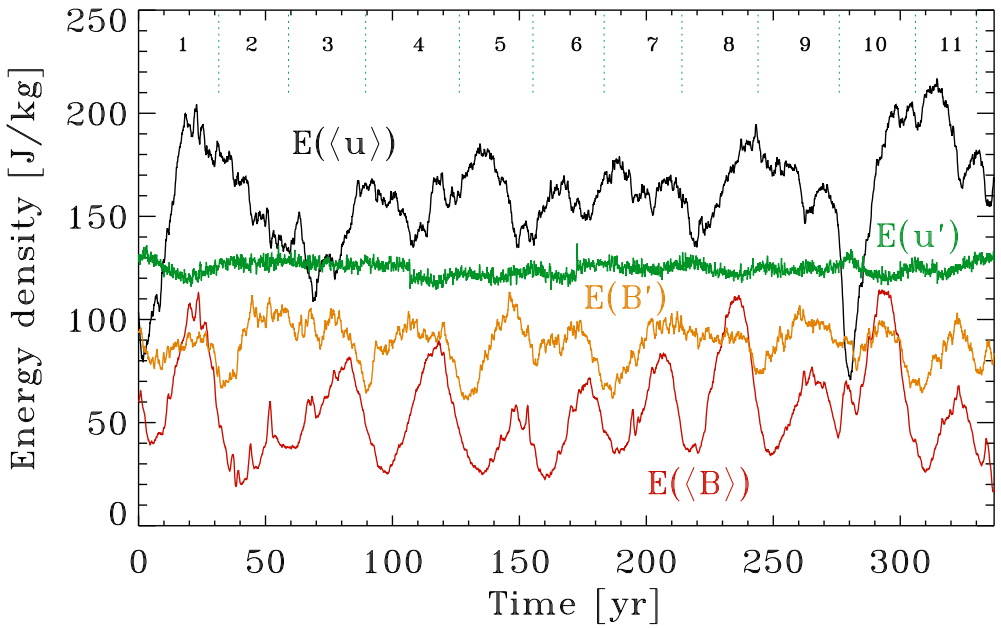

Fig. 13.— Time series of the four contributions to the global energy budget, as defined via Eqs. (33)–(36), as labeled. The 30 yr cycle shows up prominently in $E(\langle B\rangle)$, as it of course should, and also in $E(\langle u\rangle)$ but more weakly in $E(B')$ and hardly at all in $E(u')$. Note also how the large-scale flow and field are globally within a factor of two of energy equipartition at times of cycle maximum. Numbering of simulated half-cycles as on Fig. 2.